核理研研究報告　第38巻　2005年

ISSN 0385-2105

TOHOKU

# RESEARCH REPORT OF LABORATORY OF NUCLEAR SCIENCE

Vol.38 2005

TOHOKU UNIVERSITY

Editors

TAMAE, Tadaaki

OHTSUKI, Tsutomu

HAMA, Hiroyuki

Laboratory of Nuclear Science

Tohoku University

1-2-1 Mikamine, Taihaku, Sendai 982-0826

Japan

Pone: +81, 22-743-3400

Fax: +81, 22-743-3401

Web site: http://www.lns.tohoku.ac.jp/

982-0826 仙台市太白区三神峯1-2-1

東北大学大学院理学研究科

附属原子核理学研究施設

電話 022-743-3400

Fax 022-743-3401

# Preface

This issue of Research Report of Laboratory of Nuclear Science reports research activities of the LNS performed in the 2004 academic/fiscal year (April 2004, March 2005). Major research activities are based on the electron accelerator complex consisting of the 300-MeV LINAC and the 1.2-GeV STB ring. The accelerators have altogether provided a beam time of about 3,300 hours for various experiments through the year.

In this year, ( $\gamma$ , $K^0$) measurements with the NKS spectrometer finished at the experimental hall 2, where a construction of a larger spectrometer called New NKS spectrometer has been planned. A series of ( $\gamma$ , $\eta$ ) experiments have been performed with SCISSORS at the GeV $\gamma$-ray experimental hall using a new tagging photon system. The measurements on (e, e'p) reactions have also been performed at the experimental hall 2 by using a 200-MeV stretched beam extracted from the STB ring. Experiments on coherent radiation were performed by using pulsed electron beams from the LINAC. Various radioactive isotopes were produced by using high intensity beams below 50 MeV at the experimental hall 1. They were served for element analyses as well as for detailed study of decay properties.

We hope that this Report will serve as a quick overview of the present LNS activities over a variety of nuclear research fields.

Jirohta KASAGI
Director

# Research Report of Laboratory of Nuclear Science
# Volume 38, 2005

## Contents

## Ⅱ. Radiochemistry



## Ⅲ. List of Publication



## Ⅳ. Approved Experiments

# 核理研研究報告　第38巻　目　次

## Ⅰ．原子核物理



## Ⅱ．放射化学

# Ⅰ. Nuclear Physics

(LNS Experiment : #2446, #2506)

# Photoproduction of Neutral Kaons on Liquid Deuterium Target

K. Tsukada[1], T. Takahashi[1*], T. Watanabe[1†], P. Bydžovský[2], M. Ejima[1], Y. Fujii[1], K. Futatsukawa[1], O. Hashimoto[1], K. Hirose[1], T. Ishikawa[3], S. Kameoka[1‡], H. Kanda[1], F. Kato[1], S. Kinoshita[1], T. Kinoshita[3], T. Kon[1], O. Konno[5], K. Maeda[1], A. Matsumura[1], Y. Miura[1], H. Miyahara[3], H. Miyase[1], T. Nakabayashi[3], K. Nonaka[1], A. Ohtani[1], Y. Okayasu[1], M. Oyamada[1], A. Sasaki[4], H. Shimizu[3], T. Tamae[3], H. Tamura[1], T. Terasawa[3], H. Tsubota[1], S. N. Nakamura[1], H. Nomura[1], M Ukai[1§], D. Uchida[1], H. Yamauchi[1], H. Yamazaki[3], K. Yawata[1], and M. Wakamatsu[1]

[1]*Department of Physics, Tohoku University, Sendai, 980-8578*
[2]*Nuclear Physics Institute, 25068, Řež, Czech Republic*
[3]*Laboratory of Nuclear Science, Tohoku University, Sendai, 982-0826*
[4]*Department of Electrical and Electronic Engineering, Akita University, Akita, 010-8502*

We have performed the experiment of $K^0$ photoproduction on the liquid deuterium target with Neutral Kaon Spectrometer (NKS) at LNS-Tohoku. The $K^0$s were measured via $K^0_S \rightarrow \pi^+\pi^-$ decay channel in the threshold region. The momentum spectra of $K^0$ photoproduction cross sections were derived and compared with the calculations using representative models.

## §1. Introduction

The investigation of the kaon production on a nucleon by the electromagnetic interaction provides invaluable information on the strangeness production mechanism, strength of meson-baryon coupling constants and structure of hadrons, being labeled by the strangeness degree of freedom. Such studies using beams of real photons and electrons have been conducted both experimentally and theoretically since the 1950′s, taking advantage of the electromagnetic interaction that is understood better than the hadronic interaction. Until now, the experimental studies have been carried out in $p(\gamma, K^+)\Lambda$, $p(\gamma, K^+)\Sigma^0$ and $p(\gamma, K^0)\Sigma^+$ reactions among six isospin channels [1-5]. However, no data have been measured for the other three channels on a neutron. Theoretically, phenomenological models have been constructed based on measured channels so far. The isobar models, Kaon-MAID [6] and SLA [7], were adopted in the present analysis. The predictions of the photon energy dependence and the kaon angular distribution of the other three channels on a neutron using these models are quite different.

*Present address : Institute of Particle and Nuclear Studies (IPNS), High Energy Accelerator Research Organization (KEK)
†Present address : Department of Physics, Gifu University, Gfu 501-1193
‡Present address : Computing Research Center, High Enegy Accelerator Research Organization (KEK)
§Present address : Cyclotron and Radioisotope Center (CYRIC), Tohoku University, Sendai, 980-8578

The lack of the key data for strangeness photoproduction of the three channels on a neutron is due to the experimental difficulties to measure neutral kaons and to prepare a neutron target. The measurement of these three strangeness production channels provides much information on the strangeness photoproduction mechanism. In particular, the $n(\gamma, K^0)\Lambda$ reaction has following features. (1) Since no charge is involved, the $t$-channel Born term does not contribute. (2) It is a mirror reaction to $p(\gamma, K^+)\Lambda$. For the hyperon resonance exchange terms, a coupling constant, $g_{K\Sigma N}$, changes its sign from the isospin symmetry, $g_{K^0\Sigma^0 n} = -g_{K^+\Sigma^0 p}$, resulting the different interference effect. Furthermore, the number of resonances to be considered is small in the threshold region. Therefore, the $n(\gamma, K^0)\Lambda$ reaction is expected to play an essential role to investigate the strangeness photoproduction mechanism.

In this paper, we present the results of photoproduction of neutral kaons on deuterons near the threshold.

## §2. Experiment

We carried out the experiment of the $d(\gamma, K^0)$ reaction in the threshold region, $E_\gamma = 0.8 \sim 1.1$ GeV. The $K^0$s were measured in $\pi^+\pi^-$ decay mode with Neutral Kaon Spectrometer (NKS) which we installed in LNS-Tohoku. Figure 1 shows a schematic view of NKS which consists of a dipole magnet of 107 cm diameter and 60 cm gap with 0.5 T, straw drift chambers (SDC), cylindrical drift chambers (CDC), an inner hodoscope (IH), an outer hodoscope (OH) and electron veto counters (EV). The detector configuration was symmetric against the beam line. The solid angle of NKS was about $\pi$ sr. The CDC and SDC were used to measure particle momenta in the horizontal plane by trajectory reconstruction. The magnetic field map was calculated by TOSCA. IH and OH were used for the time-of-flight measurement and event triggers. The momenta and time-of-flights were used for the particle identification. As a trigger condition, we required more than two charged particles; at least one event both in the left and right arms in coincidence with a tagger signal. EVs were employed to reduce the serious background triggered by $\gamma \rightarrow e^+e^-$ conversion. They covered vertically $\pm$ 2.5 cm in the horizontal plane at OH's positions. The geometrical acceptance was reduced by 8 %.

The photon beam was generated from the 1.2 GeV electron beam via bremsstrahlung and its energy was tagged by the STB-tagger system [8]. Typical tagged photon intensity was $2 \times 10^6$/sec and tagging efficiency was $79 \pm 1$ %. Total experimental period was about 1000 hours.

In order to investigate the $K^0$ elementary production process on a neutron, the liquid deuterium target with a thickness of 3.2 cm was used. The target system was developed for this experiment and provided the stable liquid-state deuterium during the experimental period [9]. The density of the target was estimated to be 0.17 g/cm$^3$ from the temperature of the target and the pressure.

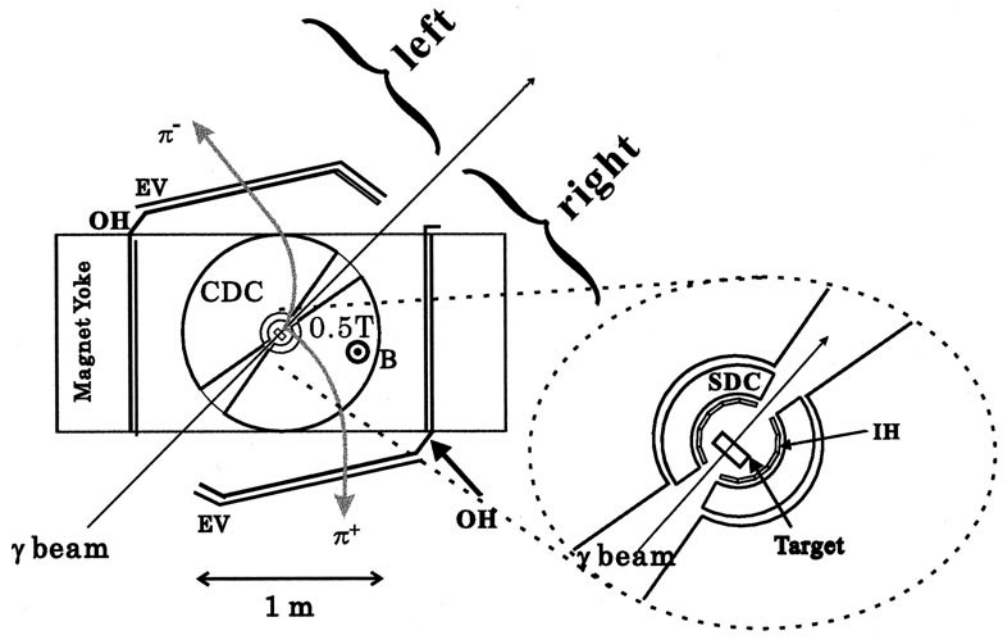


Fig.1. Schematic view of the Neutral Kaon Spectrometer (NKS).

## §3. Analysis

The momenta of particles were derived from the curvature of trajectories. Besides, the velocities of particles were calculated from the time of flight and the flight length. The $e^+e^-$ events were removed by rejecting the events of which the vertex position was upstream the target. Figure 2(a) shows the vertex point distribution of the $\pi^+\pi^-$ events. An opening angle ($\eta$) cut of $-0.9 < \cos\eta < 0.8$ was applied in order to remove the $e^+e^-$ or vertex mis-reconstruction events. The vertex resolution was estimated to be 1.3 mm in RMS in the beam direction. Most of events were originated in the target. Backgrounds through such as a multi pion productions, N* and $\rho$, whose production cross sections are much larger than that of kaon production. Hence, no peak is observed in the invariant mass spectrum as shown in Fig. 2(b) for events in the target region. $K^0$ events are enhanced by selecting vertex points in the decay volume, because $K^0_S$ has a relatively long life time of $c\tau$=2.68 cm. Figure 2(c) shows the invariant mass spectrum when events in the decay volume are chosen. The peak of $K^0_S$ is clearly seen as shown in the figure. The number of $K^0$ events is about 900 for the present data. In order to obtain the cross section, we defined the gate in the invariant mass spectrum, $0.46 \leq M(\pi^+\pi^-) < 0.54$ GeV/c$^2$. Momentum distributions of $K^0$ were obtained after subtracting background contributions. The origin of the backgrounds were considered as (1) leakage from the target region due to the finite resolution of the vertex point reconstruction, and (2) wrong combination between $\pi^+$ from $K^0$ and $\pi^-$ from $\Lambda$. The first one was estimated from the events originated in the target region, and the second one was estimated by Geant4 simulation. These estimations gave the shape of the backgrounds, and the magnitude of the backgrounds were adjusted by fitting the invariant mass spectrum. Figure 3 shows the fitting result assuming a gaussian for $K^0$ and the shapes of backgrounds as estimated in the photon energy from 0.9 to 1.0 GeV (ELow) and

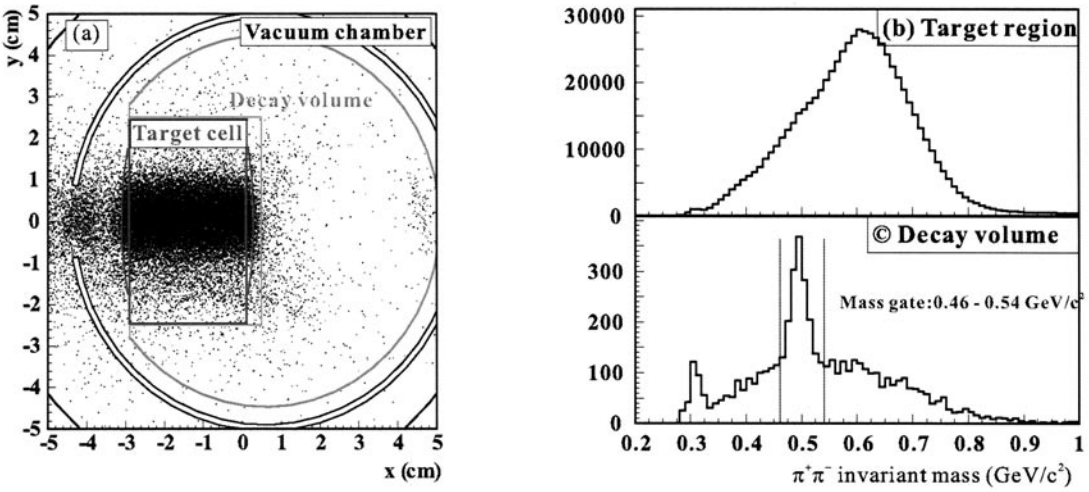


Fig.2. (a) Vertex distribution for $\pi^+\pi^-$ events. The beam comes from left to right. Events come mainly from the target region. (b), (c) An invariant mass spectrum of $\pi^+\pi^-$ events with the gate that the vertex is in the target for (b) and outside the target denoted by decay volume for (c).

form 1.0 to 1.1 GeV (EHigh).

The acceptance of NKS was calculated by a Geant4 simulation. The geometry of NKS was considered realistically, and the position and time resolution of the detectors were taken into account. Various analysis efficiencies were also estimated in the acceptance. Figure 4 shows the contour plot of the acceptance map. We used the data with momentum ($P$) and angle ($\cos\theta$) of $K^0$ in the effective regions shown in the figure because the acceptance is very low out of these regions. In this paper, the results in Region 1 are presented.

## §4. Results and Discussion

The obtained momentum spectra of $K^0$s are shown in Fig.5. The backgrounds contributions are already subtracted. The integrated momentum range is limited as mentioned in the previous section. The obtained spectra are compared with the calculations using the representative two models, Kaon-MAID [6] and Saclay-Lyon A (SLA) [7]. The lines represent calculations in the plane wave impulse approximation framework using Bonn OBEPQ (One-Boson-Exchange-Potential in Q-space) deuteron wave function [10] by Bydžovský *et al*. [11]. The Kaon-MAID model is the only model to predict the elementary cross section of $K^0$ photoproduction on a neutron assuming SU(3) symmetry. On the other hand, SLA has an adjustable parameter for $K^0\Lambda$ photoproduction, since the ratio of the decay width between the charged and neutral $K_1$ resonance ($R_{K_1^0K_1^+}$) is unknown. In Kaon-MAID, this ratio was obtained from the $\gamma + p \rightarrow K^0 + \Sigma^+$ process. Therefore, the elementary cross sections of SLA are calculated assuming various $r_{K_1K_1^+}$. Kinematical regions are also selected for the calculations similarly to the experimental data.

Since we measured only $K^0$, the $\Sigma$ production process may contribute in addition to $K^0\Lambda$ production. From the estimation using Kaon-MAID, the contributions of $\Sigma$ production are negligibly small in the

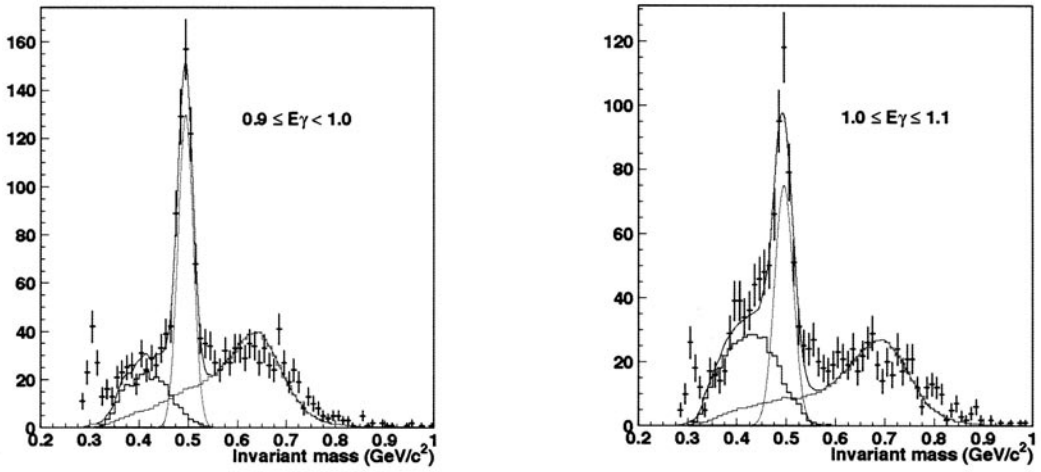


Fig.3. Fitting results of invariant mass spectra in photon regions from 0.9 to 1.0 GeV (ELow, left) and from 1.0 to 1.1 GeV (EHigh, right). The contribution around 0.4 GeV/c$^2$ comes from the wrong combination background and that around 0.6 GeV/c$^2$ comes from the leakage of the target events. The peak near 0.3 GeV/c$^2$ comes from the $e^+e^-$ events.

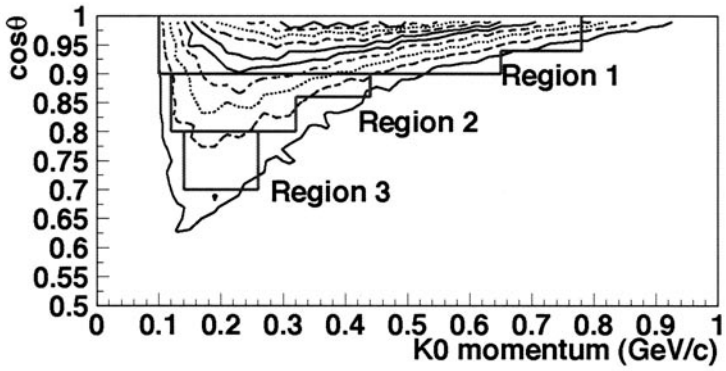


Fig.4. The contour plot of the acceptance map of NKS. The effective regions, Region 1, Region 2 and Region 3, are overdrawn by solid lines.

ELow region and sizable large at lower momentum in the EHigh region. The prediction based on the Kaon-MAID model is consistent with our data in the ELow region but too large in the EHigh region even if the Σ contribution is involved. The spectra calculated by SLA with $r_{K_1K_7} = -1.9$ well account for the present results at both energy regions.

In the ELow region, the shape of the momentum spectrum in the laboratory system mainly depends on the angular distribution in the center of mass system. From the momentum distributions using SLA with various $r_{K_1K_7}$ values, it is favored that the $K^0$ photoproduction on a neutron has a backward peak in the center of mass system.

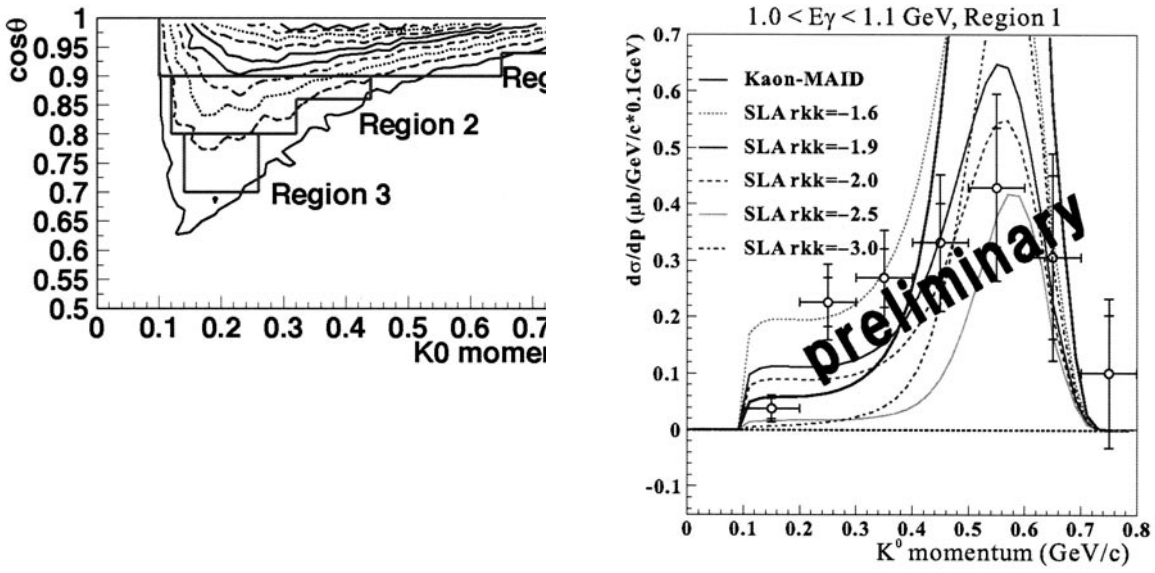


Fig.5. Momentum dependences after the correction for efficiencies and subtraction of backgrounds. The lines represent the calculations using Kaon-MAID (solid), SLA($r_{K_1K_\gamma}$= − 1.6, dotted), SLA($r_{K_1K_\gamma}$=−1.9, solid), SLA($r_{K_1K_\gamma}$=−2.0, dashed), SLA($r_{K_1K_\gamma}$=−2.5, solid) and SLA($r_{K_1K_\gamma}$=−3.0, dash-dotted). The photon energy ranges are from 0.9 to 1.0 GeV(ELow, left) and from 1.0 to 1.1 GeV(EHigh, right). Error bars are overdrawn for the (statistic) and (statistic + systematic) errors.

## §5. Summary

We have successfully measured neutral kaons, bombarding a liquid deuterium target with a photon beam in the threshold region from 0.8 to 1.1 GeV. It was the first data for $K^0$ photoproduction on the deuteron in this energy region. The momentum spectra of $K^0$ production were compared with theoretical spectra calculated assuming isobar models for the elementary process and a realistic deuteron wave function for the target nucleus. The present experiment has demonstrated the usefulness of the neutral kaon measurement for the investigation of photo strangeness production reactions.

## Acknowledgement

This work was supported by Grant-In-Aid for Scientific Research from The Ministry of Education of Japan, Nos. 09304028, 12002001, 14740150 and 16GS0201.

## References

[1] D. S. Carman *et al.*: Phys. Rev. Lett. **90** (2003) 131804.

[2] J. W. C. McNabb *et al.*: Phys. Rev. C**69** (2004) 042201.

[3] K. H. Glander *et al.*: Eur. Phys. J. A**19** (2004) 251.

[4] M. Q. Tran *et al.*: Phys. Lett. B**445** (1998) 20.

[5] R. G. T. Zegers *et al.*: Phys. Rev. Lett. **91** (2003) 092001.

[6] F. X. Lee, T. Mart, C. Bennhold, and L. E. Wright : Nucl. Phys. A**695** (2001) 237.

[7] T. Mizutani, C. Fayard, G. H. Lamot, and B. Saghai : Phys. Rev. C**58** (1998) 75.

[8] H. Yamazaki *et al*.: Nucl. Instr. and Meth. A**536** (2005) 70.

[9] H. Kanda *et al*.: Research Report of LNS, Tohoku University **37** (2004) 27.

[10] R. Machleidt, K. Holinde, and C. Elster : Phys. Rept. **149** (1987) 1.

[11] P. Bydzovsky, M. Sotona, O. Hashimoto, and T. Takahashi : private communications.

(LNS Experiment : #2371, #2397, #2413, #2433)

# Photoproduction of $\eta$-mesons off C and Cu Nuclei for Photon Energies below 1.1 GeV

T. Kinoshita[1], H. Yamazaki[1], H. Fukasawa[1], K. Hirota[1*], T. Ishikawa[1], J. Kasagi[1], A. Kato[1†], T. Katsuyama[1], K. Kino[1‡], F. Miyahara[1], T. Nakabayashi[1], K. Nawa[1], K. Okamura[1], Y. Saitoh[1], K. Satou[1], M. Sengoku[1], H. Shimizu[1], K. Suzuki[1], S. Suzuki[1], T. Terasawa[1], H. Kanda[2], K. Maeda[2], T. Takahashi[2§], Y. Aruga[3], T. Fujinoya[3], A. Iijima[3], M. Itaya[3], Y. Ito[3], T. Iwata[3], H. Kato[3], T. Kawamura[3], T. Michigami[3], M. Moriya[3], T. Sasaki[3], Y. Tajima[3], S. Takita[3], T. Noma[3], M. Yamamoto[3], H. Y. Yoshida[3], Y. Yoshida[3], O. Konno[4], T. Maruyama[5], and T. Yorita[6]

[1]*Laboratory of Nuclear Science, Tohoku University, Sendai 982-0826*
[2]*Department of Physics, Tohoku University, Sendai 980-8578*
[3]*Department of Physics, Yamagata University, Yamagata 990-8560*
[4]*Ichinoseki National College of Technology, Ichinoseki 021-8511*
[5]*College of Bioresource Sciences, Nihon University, Fujisawa 252-8510*
[6]*Japan Synchrotoron Radiation Research Institute, Mikazuki 679-5198*

The $\eta$-meson photoproduction cross sections have been measured on C and Cu targets for photon energies between 600 and 1100 MeV to investigate the behavior of the $S_{11}(1535)$ resonance in a nucleus. The excitation functions of the cross section as well as angular and momentum distributions of $\eta$-mesons are in quantitative agreement with Quantum Molecular Dynamics (QMD) model calculations, in which the $\eta$-meson emission processes other than the $S_{11}(1535)$ resonance are also incorporated as proposed in the $\eta$-MAID model. It is shown that the excitation of the $D_{15}(1675)$ resonance might play an important role for $E_\gamma > 900$ MeV.

## §1. Introduction

The behavior of hadrons in the nuclear medium is one of the most intriguing topics in hadron and nuclear physics. Photon induced reactions are advantageous to producing hadrons deeply inside a nucleus because photons are hardly absorbed. Modifications in appearances may always be observed. Most of them originate simply from the basic effects of the nuclear medium, such as the Fermi motion of nucleons, Pauli blocking of the final state and collisions with nucleons. In addition, an interesting possibility has been proposed; i.e., mass modification arising from partial restoration of chiral symmetry

*Present address : RIKEN, Wako 351-0198
†Present address : Japan Cycle Development Institute, Tokaimura 319-1194
‡Present address : Center for Nuclear Study (CNS), University of Tokyo, Wako 351-0198
§Present address : High Energy Accelerator Research Organization (KEK), Tsukuba 305-0801

in the nuclear medium [1, 2]. The effects of the mass change of the $\rho$-meson have been studied in $\rho$ photoproduction on nuclear targets [3, 4] as well as in the hadron reactions [5]. However, mass change of baryons has not been studied well except for the $\Delta$ resonance [6].

The $S_{11}(1535)$ resonance is proposed to be a candidate of the chiral partner of the ground state nucleon, and its resonance energy is expected to shift down by about 100 MeV in the nuclear medium where chiral symmetry is partially restored [2]. The $S_{11}(1535)$ resonance is known to decay into the $N\eta$ channel with a large branching ratio of 30-55% [7], while other nucleon resonances in this energy region hardly decay to the $N\eta$ channel. Therefore, the excitation and decay of the $S_{11}(1535)$ resonance is a dominant feature of the $\eta$ photoproduction off the nucleon in the region of photon energies below 1000 MeV [8, 9]. It is, thus, expected that the properties of the $S_{11}(1535)$ resonance in the nuclear medium can be studied through the $\eta$ photoproduction off nuclei.

The measurements of $A(\gamma,\eta)$ reactions have been reported by Röbig-Landau *et al*. on C, Ca, Nb and Pb for $E_\gamma < 800$ MeV [10], and by Yorita *et al*. on C, Al and Cu for $E_\gamma < 1000$ MeV [11]. In both measurements, the $S_{11}(1535)$ resonance is clearly observed in the excitation function, which can be reproduced by a calculation taking into account the basic effects of the nuclear medium with parameters deduced from the total cross section of the $\gamma p \rightarrow \eta p$ reaction. It seems, however, that the success of the interpretation of the $A(\gamma, \eta)$ reaction with the $S_{11}(1535)$ resonance alone is partially due to the lack of the quality in the previous data for $E_\gamma > 800$ MeV [11] as well as those of the $\gamma p \rightarrow \eta p$ reaction.

In the last several years, there were essential progresses in experimental and theoretical works on the reaction. For the experimental side, precise measurements for $E_\gamma > 800$ MeV have improved considerably the available data base [12-18] This led theoretical analyses to be more reliable for including contributions of all the resonances in this energy region as well as direct $\eta$ production processes. Of particular interest is the fact that both of the analyses performed by Saghai *et al*. [8] and by Chiang *et al*. [9] have come to the same conclusion that another $S_{11}$ resonance, $S_{11}(1650)$, also contributes in the total cross section of the $\gamma p \rightarrow \eta p$ reaction in such a way that the two $S_{11}$ resonances interfere destructively.

All these arguments raised the interest to study the behavior of the $S_{11}$ resonance again by measuring $A(\gamma, \eta)$ reactions with improved quality for the photon energies higher than 800 MeV. In this letter, we present the experimental results and compare them with calculations based on the Quantum Molecular Dynamics model (QMD) which is improved so as to include other processes than the $S_{11}(1535)$ resonance.

## §2. Experimental Procedure

The experiment was performed at the Laboratory of Nuclear Science (LNS) in Tohoku University by using tagged photon beams from the 1.2 GeV Stretcher-Booster Ring [19]. Two series of measurements were carried out in different setups: the first one at the photon beam line 1 in the experimental hall 2 and the second at the photon beam line 2 in the GeV-$\gamma$ experimental hall. The former tagging system is described in detail in Ref. [20] and a part of data obtained in the first series was reported in Ref. [21]. Photon beams of the same quality can be used at both beam lines. In the present work, the photon energy was covered from 600 to 850 MeV with $E_e = 920$ MeV and from 800 to

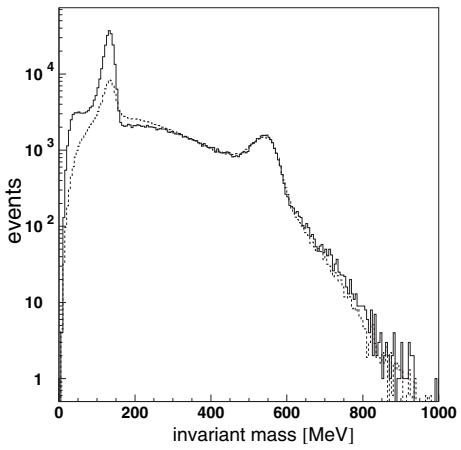


Fig.1. Invariant mass spectrum reconstructed from two photons. The solid line represents the experimental data and the dotted line the result of the simulation.

1120 MeV with $E_e = 1200$ MeV. The total tagged photon intensity was about $10^7$ Hz with a duty factor of about 80%. The size of the beam at the target position was about 6 mm (rms). The targets used were C and Cu with thicknesses of 40 and 5 mm, respectively.

Two photons from an $\eta$-meson were detected by an electromagnetic calorimeter consisting of 206 pure CsI crystals with plastic veto counters. The shape of the crystal is truncated-trapezoidal with a hexagonal cross section and its thickness is 30 cm for 148 pieces (type-A) and 25 cm for 58 pieces (type-B); the performance of the type-B is described in detail in Ref. [22]. In the first series of the measurements, they were assembled to 6 blocks and placed on three turn tables to change detector positions as reported in Ref. [22]. In the second series, they were rearranged to 4 blocks placed in such a way that two forward blocks covered angles $15° < \theta < 72°$ with respect to the beam direction and angles $-17° < \phi < 17°$ with respect to the horizontal plane and two backward blocks $95° < \theta < 125$and $-12° < \phi < 12°$ for both sides of the beam direction. The different arrangements of crystals served to check the acceptance of the detection system.

All the data were collected using a similar data acquisition system as reported in Ref. [11]. In the present work, the main trigger for the data acquisition required at least one signal from the tagging counters and two signals from the CsI detectors. The maximum counting rate of a CsI detector was about 10 kHz and that of a tagging counter was about 200 kHz. The dead time of the data taking was about 8%. A time resolution for $e$-$\gamma$ coincidences of 800 ps (FWHM) was achieved and the chance coincidence ratio was about 3%.

The $\eta$-mesons were identified via their two photon decay with an invariant mass analysis. In Fig.1, the invariant mass spectrum ($M_{\gamma\gamma}$) measured in the present work is shown by the solid line. Two prominent peaks corresponding to $\pi^0$ and $\eta$ mesons are clearly seen on the continuum background, which is considered to originate mainly from multi $\pi^0$ events. We simulated the two $\pi^0$ production process by the Monte Carlo simulation. The result is shown by the dotted line in Fig.1. The shape is well fitted with an exponential function, $\exp(aM^2_{\gamma\gamma} + bM_{\gamma\gamma})$. In order to deduce double differential cross sections, $d^2\sigma/d\theta/dp$, the invariant mass spectrum was constructed for the polar angle from 0° to 110° by 10° steps and for the momentum from 0 to 1100 MeV by 100 MeV steps. The yield of $\eta$-mesons in each spectrum was

deduced by subtracting the background events in the $\eta$ mass region, which were estimated with the function fitted to the continuum for each bin of the incident photon energy and the $\eta$-meson polar angle and momentum. Absolute cross sections were deduced by taking into the account a thickness of the targets, counts of tagging counters, a tagging efficiency, a geometrical acceptance and a branching ratio ($\eta \rightarrow \gamma\gamma$) [7]. The tagging efficiency was measured with a total absorbing lead glass detector positioned in the direct beam. The geometrical acceptance of the detection system was calculated by the Monte Carlo simulation based on GEANT3 [23]. The systematic uncertainties of the overall normalization come from the photon flux (1%), the background determination (5%) and the geometrical acceptance (5%). Consequently the overall systematic uncertainty is 7%.

## §3. Results and Discussion

Differential cross sections of the $(\gamma,\eta)$ reaction were deduced for the polar angles from 0° to 110° with respect to the photon beam direction by integrating the double differential cross sections. We show excitation functions of the $\eta$ photoproduction cross section, which were deduced by integrating differential cross sections for $0^\circ < \theta < 110^\circ$, on C and Cu targets in Fig.52(a) and 2(b), respectively. Missing yields for $\theta > 110°$ were estimated to be 2% of the integrated values at most, and the total cross section in the present work is the angle integrated one. For comparisons, also plotted are the previously reported data on C indicated with open squares up to 800 MeV [10] and with open circles up to 1000 MeV [11] and on Cu with open circles up to 1000 MeV [11]. It can be said that the present data and the reported ones are in good agreement. Moreover, the statistical accuracy is much improved for the photon energies higher than 800 MeV. The shape of the total cross sections for C and Cu is quite similar as expected. The cross section increases rapidly from the threshold energy (561 MeV for C and 550 MeV for Cu), shows a broad bump structure which has the maximum at around 850 MeV, and gradually decreases as the photon energy increases. This trend has been known from the previous investigations [11] to be basically due to the excitation of the $S_{11}(1535)$ resonance in a nucleus. The present data for C and Cu may serve for detailed comparisons with model calculations.

In Fig.2(c), ratios of the cross section of Cu to that of C ($\sigma_{Cu}/\sigma_C$) are plotted against the photon energy. One can roughly say that the observed $\eta$-mesons are mainly emitted from the surface region of the nucleus and those emitted in the deeper region are absorbed in the nuclear medium, since the ratios are close to 3.05 (the dotted line), corresponding to the ratio of $A^{2/3}$ for Cu to C. However, there exist non-negligible and systematic deviations from the $A^{2/3}$ dependence for photon energies larger than 800 MeV; the ratio becomes about 3.5 at about 900 MeV. This requires more careful and detailed analysis.

In order to explain the present data, we have performed a QMD model calculation in a different way from the previous one [11] as follows. At first, the proton and the neutron are treated independently so as to see the effect of the difference of the elementary cross sections for $\gamma p \rightarrow \eta p$ and $\gamma n \rightarrow \eta n$. This modification is necessary, because a rather large difference between the total cross sections of $\gamma p \rightarrow \eta p$ and $\gamma n \rightarrow \eta n$ has been predicted by the unitary isobar model, $\eta$-MAID [9]. The simple relation $\sigma(\gamma n \rightarrow \eta n)/\sigma(\gamma p \rightarrow \eta p) = 2/3$, established empirically for $E_\gamma < 800$ MeV [25] and used in the previous model calculations [11, 24], might not be correct at the higher energy region. Secondly, the effect of the interference between two $S_{11}$

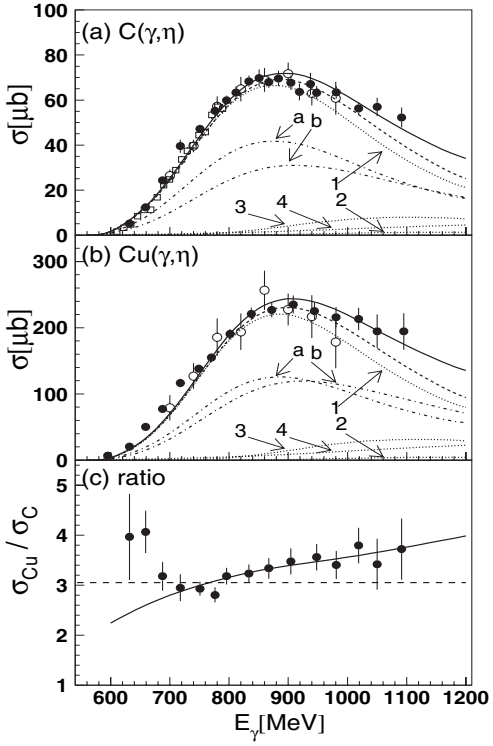


Fig.2. Cross sections of $\eta$ photoproduction measured on C(a) and Cu(b). The data measured in the present work are indicated by the solid circles, those at KEK [11] by the open circles and at Mainz [10] by the squares. The solid line is the result of the present QMD calculation. Contributions of various processes are plotted by the dotted lines labeled with numbers; label 1 for the double $S_{11}$ resonance, label 2 for the $P_{11}(1710)$, label 3 for the $D_{15}(1675)$, and label 4 for the direct processes. The dot-dashed lines are contributions due to protons (label a) and neutrons (label b). The calculation in the previous work by Yorita *et al*. [11] is plotted by the dashed line. (c) Ratio of the cross section of the Cu($\gamma$, $\eta$) reaction to that of the C($\gamma$, $\eta$) reaction. The dashed line shows the ratio of $A^{2/3}$ ($A$: mass number) and the solid line is the result of the QMD calculation.

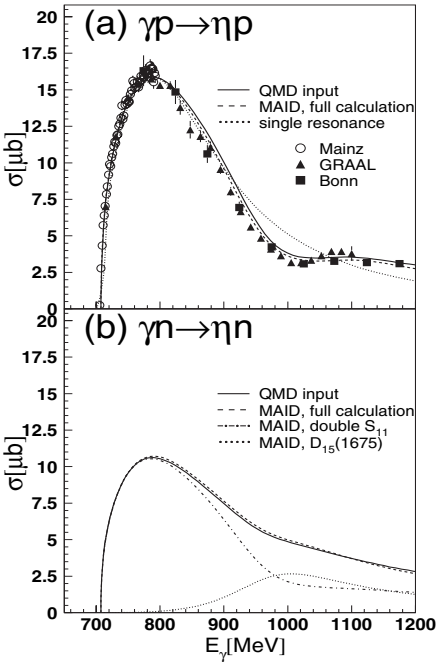


Fig.3. Excitation functions of cross sections for the elementary reaction by calculation based on the $\eta$-MAID: (a) the $\gamma p \rightarrow \eta p$ reaction and (b) the $\gamma n \rightarrow \eta n$ reaction. The solid lines are used in the present QMD calculation and the dashed lines are the results of the full $\eta$-MAID including all the resonances and the direct process. In (a), the excitation function used in the previous work by Yorita *et al*. [11] is also plotted by the dotted line as well as experimental data from Mainz [12], GRAAL [16] and Bonn [18]. In (b), contributions of the two resonances, $S_{11}(1535)$ and $S_{11}(1650)$, destructively interfered, are shown by the dot-dashed line, while that of the $D_{15}(1675)$ is shown by the dotted line.

resonances in this energy region, $S_{11}(1535)$ and $S_{11}(1650)$, is included in the calculation as the form of the cross section. The reason of this modification is as follows. Saghai *et al*. [8] and Chiang *et al*. [9] analyzed the total cross section of the $\gamma p \rightarrow \eta p$ reaction. They came to the same conclusion that the experimentally observed cross section below 1100 MeV is not only due to the $S_{11}(1535)$ resonance but also due to the $S_{11}(1650)$, and both resonances make a destructive interference in the cross section of $\eta$ production off the nucleon. In the present QMD calculation, it is impossible to treat directly the transition amplitudes, and, thus, the calculated cross section including a destructive interference term is incorporated instead

of an incoherent sum of two single resonances which cannot reproduce the experimental data well.

In Fig.3, the total cross sections of the $N(\gamma, \eta)$ reaction are shown in order to explain input quantities to the present QMD calculations. The experimental cross sections of the $\gamma p \rightarrow \eta p$ reaction are shown in Fig.3(a); data plotted with circles from Ref. [12], triangles from Ref. [16] and squares from Ref. [18]. Also shown are the results of the $\eta$-MAID calculation, on which we have based for the elementary cross section. The characteristic feature of the experimental data is a broad peak followed by a flat region with a small dip at 1010 MeV. The single resonance excitation can reproduce only the broad resonance shape but fails to reproduce the dip and flat as indicated by the dotted line, which corresponds to the elementary cross section used in our previous analyses [11]. The dashed line is the result of the full $\eta$-MAID calculation which includes all the resonances in this energy region with direct $\eta$ production processes. As mentioned above, the essential point is the destructive interference of the $S_{11}(1535)$ and the $S_{11}(1650)$ resonances, which reproduces the dip and flat behavior very well. Another non-negligible process is the excitation of the $P_{11}(1710)$ resonance, which slightly contributes to the flat region around 1100 MeV. Therefore, we have included three resonance excitations, $S_{11}(1535)$, $S_{11}(1650)$, and, $P_{11}(1710)$ and the direct processes in the cross section of the $\gamma p \rightarrow \eta p$ reaction for the QMD calculation. The total cross section of the elementary $\gamma p \rightarrow \eta p$ reaction is calculated practically by summing up the cross sections of the double $S_{11}$, the $P_{11}$, and the direct processes, although the exact calculation should be the square of sum of the amplitude of each process. The solid line in Fig.3(a) is the elementary $\gamma p \rightarrow \eta p$ cross section used in the present QMD calculation, being slightly larger than the full calculation of the $\eta$-MAID.

For the cross section of the $\gamma n \rightarrow \eta n$ reaction, no experimental data have been reported so far. We, again, follow the $\eta$-MAID calculation as shown in Fig.3(b). The dashed line corresponds to the full calculation of the $\eta$-MAID including all the resonances and the direct processes. We select the double $S_{11}$ resonance, the $D_{15}(1675)$ resonance as major processes of excitations and the direct processes for the QMD input. The $\eta$-MAID calculation predicts rather large cross sections through the $D_{15}(1675)$ resonance excitation, which is essentially prohibited in the $\gamma p \rightarrow \eta p$ reaction by the Moorhouse selection rule [26]. The cross section through the two $S_{11}$ resonances is calculated with the destructive interference term. It shows a dip at around 1000 MeV as shown by the dot-dashed line in Fig.3(b), where one sees that a large contribution from the $D_{15}(1675)$ resonance, which is plotted by the dotted lines, fills the dip and appears like a shoulder of the $S_{11}(1535)$ resonance. The sum of the cross sections of the selected processes, which is employed as the elementary $\gamma n \rightarrow \eta n$ reaction, is shown by the solid line. The difference from the full calculation is very small as in the case for the $\gamma n \rightarrow \eta n$ reaction.

Having discussed the elementary cross sections, we now return to the C$(\gamma, \eta)$ and Cu$(\gamma, \eta)$ reactions. In Figs.2(a) and 2(b), the cross sections obtained in the present work are compared with the QMD calculations. As mentioned above, the elementary cross sections of the $\gamma p \rightarrow \eta p$ and $\gamma n \rightarrow \eta n$ reactions are treated independently; they are the solid lines in Fig.3(a) and Fig.3(b) for proton and neutron, respectively. The $\eta$-emission probability through the resonance excitation is calculated according to the Breit-Wigner resonance formula for the $P_{11}(1710)$ and the $D_{15}(1675)$ resonances. For the $S_{11}$ resonance excitation in the present work, however, the cross section including the interference of the two $S_{11}$ resonances is used as if a resonance of the mixed state which is not described by the single Breit-Wigner

Table 1. Parameters of nucleon resonances used in our calculation. $A^{p,n}_{1/2,3/2}$ are photoexcitation helicity amplitudes of nucleon resonances and $\beta_{\eta N}$ is $N\eta$ decay branching ratio. Those in the last columm are used in the previous analysis [11].

| N* | Mass [Mev] | Width [Mev] | $\beta_{\eta N}$ [%] | $A^{p}_{1/2}$ | $A^{p,n}_{3/2}$ $[10^{-3}\mathrm{GeV}^{-1/2}]$ | $A^{n}_{3/2}$ |
|---|---|---|---|---|---|---|
| $S_{11}(1535)$ | 1541 | 191 | 50 | +118 | − | − |
| $S_{11}(1710)$ | 1638 | 114 | 7.9 | +68 | − | − |
| $P_{11}(1710)$ | 1721 | 100 | 26 | +23 | − | − |
| $D_{15}(1675)$ | 1665 | 150 | 17 | 0 | 0 | − 58 |
| $S_{11}(1535)$ | 1542 | 150 | 55 | +102 | − | − |

formula is excited, and the lifetime and the decay branch of the $S_{11}(1535)$ resonance is applied to the mixed state. This approximation seems to be allowed, since the $\eta$-meson is mainly emitted via the $S_{11}(1535)$ resonance. The resonance parameters in the $\eta$-MAID are used for each resonance, and are summarized in Table 1.

It should be noticed for the QMD calculations in the present work that the effective energies of the incident channel are calculated for each photon-nucleon collision with a nucleon bound in a mean field potential. The effective energy which results in the reduction of the $\eta$ yield for the threshold region has been discussed [24,27] and the result of such calculation improves the reproduction of the cross sections below 800 MeV. Thus, we have calculated the effective total energy followed as $W = \sqrt{s} - U$, where $W$ is the effective total energy, $\sqrt{s}$ is the c.m. energy of the incident photon and a nucleon in the nucleus and $U$ is the nucleon potential calculated from the mean field potential in Ref. [28]. As described in Ref. [11], the Fermi motion of nucleons, the Pauli blocking, collisions of nucleon resonances with nucleons and the absorption of the $\eta$-mesons are taken into account in the calculation.

In Fig.2(a) and 2(b), the dashed line is the results of the QMD calculation in which only the $S_{11}(1535)$ resonance is incorporated with the assumption of $\sigma_n/\sigma_p = 2/3$. This corresponds to the previous calculation in Ref. [11]. For both C($\gamma$, $\eta$) and Cu($\gamma$, $\eta$) reactions, the calculation reproduces data up to 950MeV. However, it underestimates the yield for $E_\gamma > 1000$ MeV. The solid line corresponding to the new recipe covers the deficit and reproduces the data well up to 1100 MeV. Contributions of each process are also shown in Fig.2(a) and 2(b). As can be seen, in addition to the largest contribution of the double $S_{11}$ resonance indicated by the dotted line 1, the contributions of the $D_{15}(1675)$ resonance and the direct processes are expected for $E_\gamma > 900$ MeV. The present calculation suggests that more than 18% of the cross section at 1000 MeV originates from other processes than the excitation of the $S_{11}$ resonances. It is of particular interest that the $D_{15}(1675)$ resonance plays an important role for higher photon energies, since only neutrons can be excited in a naive quark model. The dot-dashed lines labeled a and b in Fig.2 correspond to the contributions of protons and of neutrons, respectively. The ratio of the contribution of neutrons to that of protons is nearly 0.67 for C and 0.84 for Cu at $E_\gamma < 800$ MeV, where only the $S_{11}$ resonance formation process can contribute, and becomes 0.97 for C and 1.23 for Cu at around $E_\gamma = 1100$ MeV due to the existence of the $D_{15}(1675)$ resonance. The change of the contribution of neutrons to protons may explain the change of the ratio of the total cross section $\sigma_{Cu}/\sigma_C$ plotted in Fig.2(c), where the calculated ratio is also shown by the solid line. The calculation explains the trend of the ratio very well, although it fails for the lowest two points.

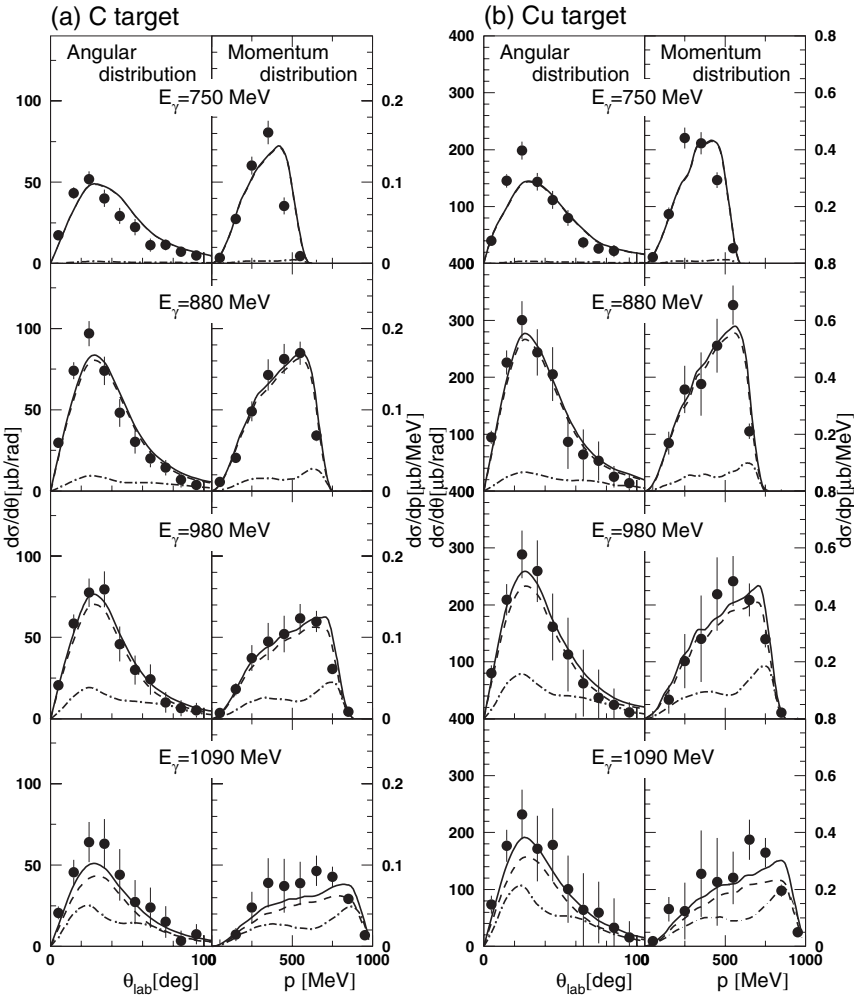


Fig.4. Angular distributions, $d\sigma/d\theta$, and momentum distributions, $d\sigma/dp$, of the $(\gamma, \eta)$ reaction measured on C (a) and Cu (b). The present results are plotted with the closed circles for $E_\gamma$ = 750, 880, 1000, and 1100 MeV. The solid line is the result of the QMD calculation and the dashed one represents without the contribution of $D_{15}(1675)$, and the dot-dashed line shows only the contribution of $D_{15}(1675)$ resonance multiplied by 4.

The above discussion on Fig.2 requires at least the following; the elementary cross section of the $\gamma n \rightarrow \eta n$ reaction exceeds that of the $\gamma p \rightarrow \eta p$ for $E_\gamma > 1000$ MeV, due to another process besides the $S_{11}$ resonance formation. Recently, Kuznetsov *et al*. reported the $n\eta$ and $p\eta$ coincidence measurements in the D$(\gamma, \eta)$ reaction [29]. Their result that yields of the $n\eta$ coincidence events are larger than those of the $p\eta$ events at around 1000 MeV is consistent with the present interpretation.

Additional effects that might possibly give rise deviations from the pure $S_{11}$ resonance formation may be seen in the angular and momentum distributions of the emitted $\eta$-mesons. They are shown in Fig.4 for $E_\gamma$ = 750, 880, 980, and 1090 MeV, and compared with the QMD calculations. The results for the C target are shown in Fig.4(a), and the Cu target in Fig.4(b). All the angular distribution data show a broad structure peaked at around 30°. This is a characteristic of the quasi-free *s-wave* $\eta$ production. The solid lines in the figures are the results of the QMD calculation, and the experimental data for both angular and momentum distributions are essentially well reproduced by the corresponding calculations. The dashed

lines shows the results without the contribution of the $D_{15}(1675)$ resonance and the dot-dashed lines correspond to the contribution of the $D_{15}(1675)$ resonance multiplied by 4. As shown, the contribution of the $D_{15}(1675)$ resonance has a different structure in these distributions because of the *d-wave* $\eta$ emission. Since the contribution of the $D_{15}(1675)$ resonance is not large, the present data, unfortunately, cannot give a firm evidence for the excitation of the $D_{15}(1675)$ resonance in both reactions.

As we have discussed above, the comparison of new data with the QMD model calculations suggests strongly that the cross sections of $\eta$ photoproduction off nuclei contain non-negligible quantities through the process other than the $S_{11}(1535)$ resonance formation for the photon energies above 850 MeV. Thus, in order to investigate the change of the $S_{11}$ properties in the nuclear medium such as the mass shift proposed in Ref. [2], one needs precise data of the cross section for the $\gamma n \rightarrow \eta n$ reaction. The present work has shown that the use of the elementary cross sections of $\eta$-MAID can reproduce the experimental data very well but remains an interesting subject for future investigations.

## §4. Conclusion

In summary, the $\eta$ photoproduction cross sections were measured on the C and Cu targets for the photon energies between 600 and 1100 MeV. The excitation functions of the total cross section as well as angular and momentum distributions were in quantitative agreement with the QMD model calculations in which the cross sections proposed in the $\eta$-MAID model were used for the elementary reactions $\gamma p \rightarrow \eta p$ and $\gamma n \rightarrow \eta n$. The agreement suggests that there is a difference in the shape of the cross sections between proton and neutron in a nucleus. In order to discuss the change of the properties of the $S_{11}(1535)$ resonance, the cross section of the $\gamma n \rightarrow \eta n$ reaction experimentally measured is highly desirable to be incorporated in the model calculations.

## Acknowledgements

We would like to thank the accelerator staff at LNS for their support during the experiment. This work was partly supported by the Grant-in-Aid for Scientific Research (Nos. 1040067, 07740197, and 15340069) of the Ministry of Education of Japan.

## Reference

[1] T. Hatsuda and S. H. Lee: Phys. Rev. C**46** (1992) 34.

[2] H. C. Kim, D. Jido, and M. Oka: Nucl. Phys. A**640** (1998) 77;
D. Jido, Y. Nemoto, M. Oka, and A. Hosaka: Nucl. Phys. A**671** (2000) 471;
D. Jido, T. Hatsuda, and T. Kunihiro: Phys. Rev. Left. **84** (2000) 3252.

[3] G. J. Lolos *et al*.: Phys. Rev. Lett. **80** (1998).

[4] B. Krusche *et al*.: Phys. Rev. Lett. **86** (2001) 4764.

[5] G. Agkichiev *et al*.: Phys. Rev. Lett B**422** (1998) 405;
D. Adamova *et al*.: Phys. Rev. Lett. **91** (2003) 042301.

[6] E. L. Hjort *et al*.: Phys. Rev. Lett. **79** (1997) 4345;

D. Plete *et al*.: Z. Phys A**359** (1997) 55.

[7] S. Eidelman *et al*., (Particle Date Group): Phys. Lett. B**592** (2004) 1.

[8] B. Saghai and Z. Li: Eur. Phys. J. A**11** (2001) 217.

[9] G. Knöchlein, D. Drechsel, and L. Tiator: Z. Phys. A**352** (1995) 327;

[10] M. Röbig-Laudau *et al*.: Phys. Lett. B**373** (1996) 45.

[11] T. Yorita *et al*.: Phys. Lett. B**476** (2000) 226;
H. Yamazaki et al.: Nucl. Phys. A670 (2000) 202c.

[12] B. Krusche *et al*.: Phys. Rev. Lett. **74** (1995) 3736.

[13] J. Ajaka *et al*.: Phys. Rev. Lett. **81** (1998) 1797.

[14] C. S. Armstrong *et al*.: Phys. Rev. D**60** (1999) 052004.

[15] R. Thompson *et al*.: Phys. Rev. Lett. **86** (2001) 1702.

[16] F. Renard *et al*.: Phys. Lett. B**528** (2002) 215.

[17] M. Dugger *et al*.: Phys Rev. Lett. **89** (2002) 222002.

[18] V. Credé *et al*.: Phys. Rev. Lett. **94** (2005) 012004.

[19] F. Hinode *et al*.: Proceedings of the 2005 Particle Accelerator Conf., Knoxville, TN, U.S.A., To be published;
H. Hama *et al*.: Proceeding of the 18th International Conference on High Energy Accelerators (HEACC2001), Tsukuba, March 2001.

[20] H. Yamazaki *et al*.: Nucl. Instr. Meth A**536** (2005) 70.

[21] H. Yamazaki *et al*.: Proceedings of the International Workshop on Physics with Gev Electrons and Gamma Rays, Sendai, Japan, February, 2001, Universal Academy Press, Inc. pp. 151;
J. Kasagi: Prog. Theo. Phys. Suppl. **149** (2003) 215.

[22] H. Okuno *et al*.: Nucl. Instr. Meth. A**365** (1995) 352;
H. Yamazaki *et al*.: Nucl. Instr. Meth. A**391** (1997) 427.

[23] CERN Program Library Long Writeup W5013: Geant Detector Description and Simulation Tool, (1993).

[24] J. Lehr, M. Post, U. Mosel: Phys. Rev. C**68** (2003) 044601.

[25] B. Krusche *et al*.: Phys. Lett. B**358** (1995) 40.

[26] R. G. Moorhouse: Phys. Rev. Lett. **16** (1966) 772.

[27] T. Maruyama, S. Chiba: Prog. Theor. Phys. **111** (2004) 229.

[28] K. Niita *et al*.: Phys. Rev. C**52** (1995) 2620.

[29] V. Kuznetsov *et al*.: hep-ex / 0409032.

(LNS Experiment : #2507)

# Comparison of the $^{40}$Ca(e, e′p) Cross Section at Low Momentum Transfer Region with Relativistic Calculations

R. Hashimoto[1], T. Tamae[1], T. Fujibayashi[2], O. Hashimoto[2], K. Hirose[2], T. Ishikawa[1], H. Kanda[2], O. Konno[3], K. Maeda[2], H. Miyase[2], S.N. Nakamura[2], M. Nanao[1], I. Nishikawa[1], T. Otsuki[1], T. Saito[4], Y. Sato[1], K. Takahashi[2], H. Tamura[2], H. Tsubota[2], M. Wakamatsu[2], H. Yamazaki[1], and H. Yuki[1]

[1]*Laboratory of Nuclear Science, Tohoku University, Sendai 982-0826*
[2]*Department of Physics, Tohoku University, Sendai 980-8578*
[3]*Department of Electrical Engineering, Ichinoseki National College of Technology, Ichinoseki 021-8511*
[4]*Faculty of Engineering, Tohoku Gakuin University, Tagajo, 985-8537*

The (e, e′$p_0$) cross section of $^{40}$Ca measured using a 199.53 MeV continuous electron beam is compared with theoretical calculations based on the relativistic distorted-wave impulse approximation (RDWIA). The theoretical values overestimate the experimental ones by a factor of 2 when the spectroscopic factor is obtained from the (e, e′p) experiment in parallel kinematics, or by a factor of 1.4 when spectroscopic factor is obtained in constant ($\omega$, $q$) kinematics.

## §1. Introduction

Recently, the (e, e′p) reaction in the quasi-elastic region and the ($\gamma$, p) reaction above the giant resonance region have been investigated in the relativistic framework [1-3]. The contributions of meson exchange currents (MEC) and the choice of the one-body current operator were discussed in Refs. [1, 2].

In previous reports [4-6] we compared the reduced cross section obtained from $^{12}$C(e, e′$p_0$) and the differential cross section obtained from $^{16}$O(e, e′$p_0$) with theoretical calculations based on the relativistic distorted wave impulse approximation (RDWIA). Both experiments were performed at a low momentum transfer region: energy transfer $\omega$ = 60 MeV and momentum transfer $|\vec{q}|$ = 105.2 MeV/$c$. The result of these reports was that RDWIA overestimates the experimental data by a factor of 2. A large contribution of the two-body seagull term was observed at high missing momentum region.

To investigate this reaction mechanism further, we choose $^{40}$Ca as a target and performed the experiment. The $^{40}$Ca(e, e′$p_0$) cross section obtained from this experiment is compared with calculations based on RDWIA.

## §2. Experiment

The experiment was performed at Laboratory of Nuclear Science, Tohoku University (LNS) using a 199.53 MeV continuous electron beam from the stretcher-booster (STB) ring. Incident electrons were scattered with a natural calcium target of 19.0 mg/cm$^2$ thickness. Scattered electrons were analyzed

their momentum at $\theta_e = 30°$ by a magnetic spectrometer (LDM) and detected with a vertical drift chamber (VDC) placed on the focal plane of the spectrometer and with a backup counter, layered three plastic scintillators behind the VDC. In this setup, $\omega$ is 60.0 ± 4.2 MeV and $|\vec{q}|$ is 105.2 MeV/$c$. Knocked-out protons were detected by SSD telescopes, which consisted of three layers of 1mm-thick SSD′s. In order to degrade the energy of protons, a 6mm-thick aluminum disk was put in front of each telescope.

The normalization of our measured (e, e′p) cross section was performed by comparing the elastic scattering cross section with that of Ref. [7]. We measured the elastic scattering cross section at $\theta_e = 58.5°$. The form factor of our experiment corresponds to that at $\theta_e = 46.0°$ with a beam energy 249.3 MeV of Ref. [7].

## §3. Result and Discussion

The measured cross sections are shown in Table 1 and Fig.1. The $^{40}$Ca(e, e′$p_0$) cross section obtained from our experiment is compared with theoretical calculations based on RDWIA [8]. The RDWIA treatment is same as in Refs. [1, 2]. The bound state wave function is a solution of a relativistic Hartree-Bogoliubov equation using parameters NLSH [9]. The EDAD1 optical potential parameters [10] are used for calculations of the scattering wave function. As the choice of the electromagnetic operator is arbitrary, three current conservation operators, cc1, cc2 and cc3, are used in the calculations.

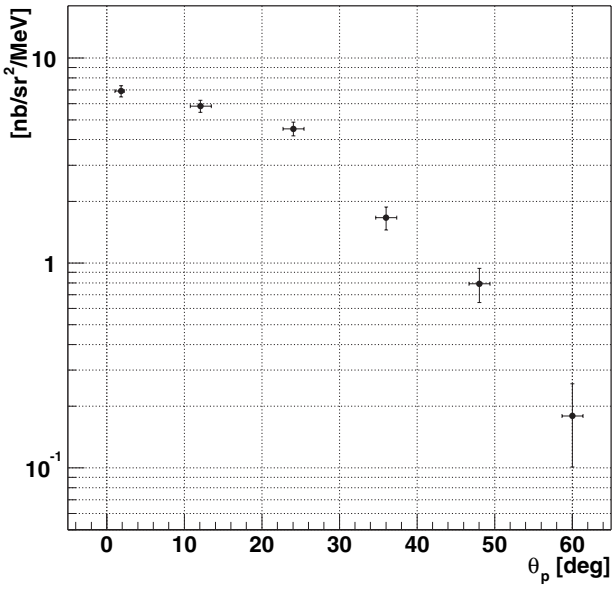


Fig.1. The $^{40}$Ca(e, e′$p_0$) cross section.

The spectroscopic factor Z($d_{3/2}$) was obtained from analysis of the quasi-elastic (e, e′$p_0$) reaction [11], which included the results of two different kinematics, parallel kinematics and constant ($\omega$, q) kinematics. The factor was calculated for the three current operators on each kinematics. The spectroscopic factors obtained from parallel kinematics and constant ($\omega$, q) kinematics are listed in Table 2. The present data are compared with

Table 1. Differential cross section of the $^{40}$Ca(e, e′$p_0$) reaction.

| $\theta_e$ | Cross section [nb/MeV/sr$^2$] |
|---|---|
| 0° | 6.901 ± 0.427 |
| 12° | 5.832 ± 0.392 |
| 24° | 4.512 ± 0.347 |
| 36° | 1.662 ± 0.213 |
| 48° | 0.791 ± 0.150 |
| 60° | 0.179 ± 0.078 |

Table 2. Spectroscopic factors for three current operators in two kinematics.

| | parallel kinematics | constant ($\omega$ , q) |
|---|---|---|
| cc1 | 0.627 | 0.446 |
| cc2 | 0.713 | 0.594 |
| cc3 | 0.766 | 0.701 |

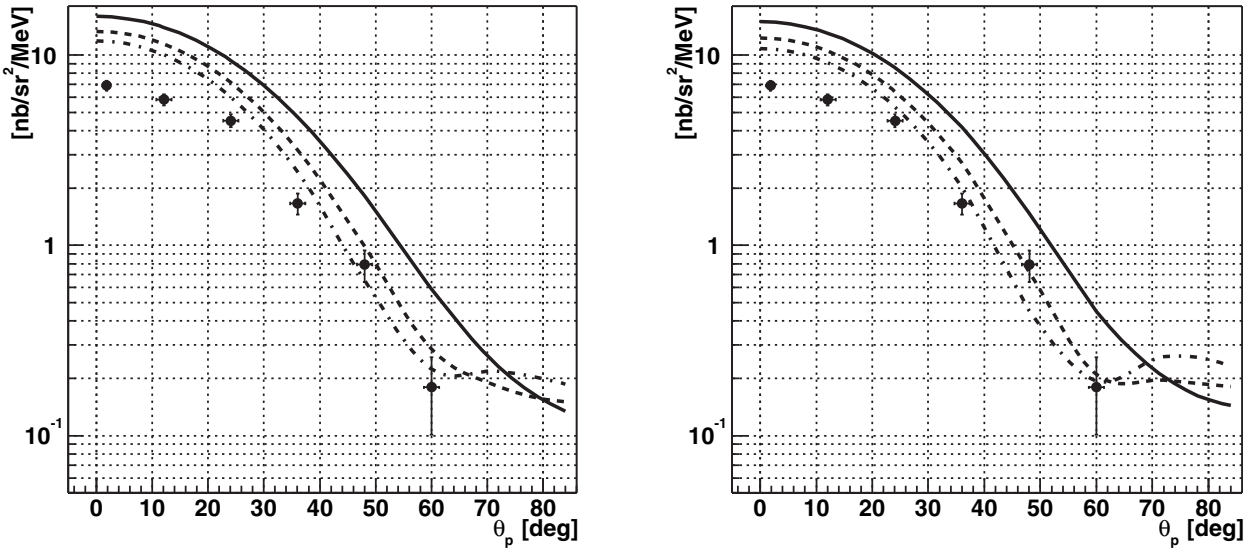


Fig.2. The $^{40}$Ca(e, e′p$_0$) cross section compared with theoretical calculations, using spectroscopic factors obtained from the (e, e′p) experiment in the parallel kinematics. Calculations include the MEC effect in the left panel, and does not in the right panel. Closed circles show the present data, and solid, dashed, and dot-dashed lines represent theoretical calculations with cc1, cc2, and cc3 current operators, respectively. $\theta_p$ is the out-going angle of the proton.

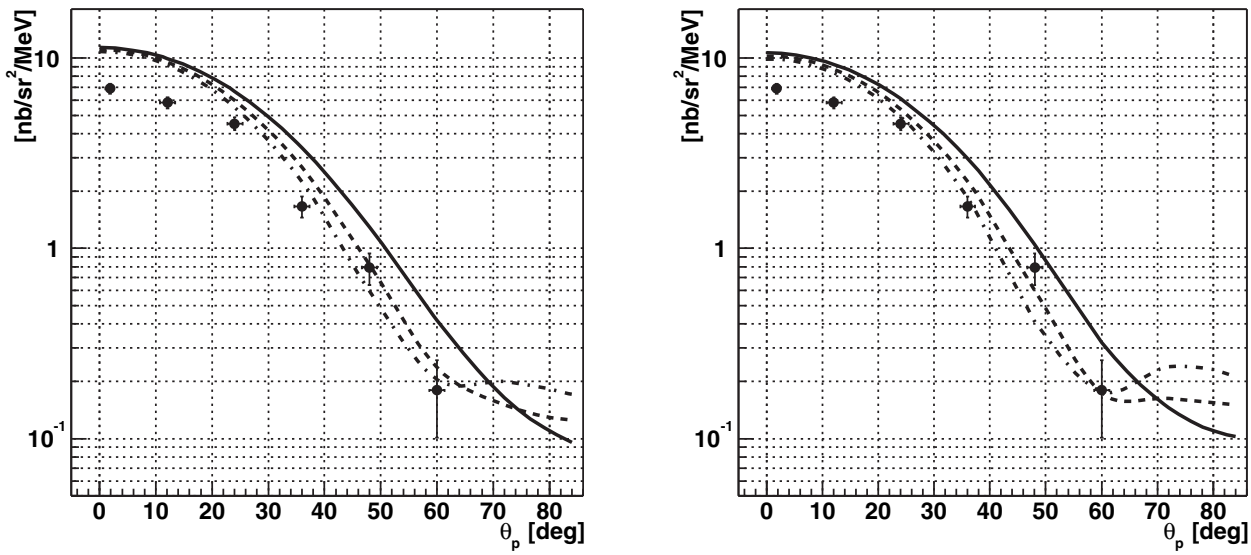


Fig.3. Same as Fig. 2, but comparison with theoretical calculations using the spectroscopic factor obtained from the (e, e′p) experiment in the constant ($\omega$, $q$) kinematics.

theoretical calculations in Figs.2 and 3. The theoretical values are obtained using 3 one-body current-conservation operators and spectroscopic factors listed in Table 2. According to Figs.2 and 3, the MEC effect is not important in the small $\theta_p$ region, corresponding to the lower momentum transfer region. Calculations with spectroscopic factors obtained from parallel kinematics overestimate the data, at forward angles, and are different from each other, as shown in Fig.2. In order to fit calculations to the data, a normalizing factor 0.423 is needed for the cc1 current, and 0.523 and 0.588 for the cc2 and, cc3 currents, respectively. Thus, theoretical values overestimate the experimental ones by a factor about 2. This result is same as in previous reports [4-6]. As shown in Fig.3, calculations with spectroscopic factors obtained from constant ($\omega$ , $q$) kinematics also overestimate the data by a factor of about 1.4, but the calculation is equivalent to each other in the small $\theta_p$ region. The theoretical values are closer to the experimental one than using a spectroscopic factor obtained in parallel kinematics, but still too large.

## §4. Summary

Both theoretical calculations using the spectroscopic factor obtained in the parallel and constant ($\omega$, $q$) kinematics. overestimate the experimental cross section, about factors 2 or 1.4, respectively. The (e, e′p) experiment at the low momentum transfer in $^{12}$C, $^{16}$O and $^{40}$Ca show some important contributions is missing in the theoretical approach.

The authors would like to thank C. Giusti and A. Meucci for their relativistic calculations. They also thank the accelerator group, the computer group and Mr. Matsuda for their assistance to the experiment. This work has been supported by Grant-in-Aid for Scientific Research (KAKENHI) (No.14540239, No.17540229) from Japan Society for the Promotion of Science (JSPS).

## References

[1] A. Meucci, C. Giusti, and F. D. Pacati: Phys. Rev. C**64** (2001) 064615.
[2] A. Meucci, C. Giusti, and F. D. Pacati: Phys. Rev. C**66** (2002) 034610.
[3] J. I. Johansson, H. S. Sherif, and G. M. Lotz : Nucl. Phys. A**605** (1996) 517.
[4] Y. Sato *et al*.: Research Report of LNS, Tohoku Univ. **33** (2000) 7.
[5] T. Tamae *et al*.: Research Report of LNS, Tohoku Univ. **36** (2003) 19.
[6] Y. Hayashi *et al*.: Research Report of LNS, Tohoku Univ. **37** (2004) 1.
[7] B. B. P. Sinha *et al*.: Phys Rev C**7** (1973) 1930.
[8] C. Giusti and A. Meucci: private communication.
[9] M. M. Shaeme, M. A. Nagarajan, and P. Ring: Phys. Lett. B**312** (1993) 377.
[10] E. D. Cooper *et al*.: Phys. Rev. C**47** (1993) 297.
[11] G. J. Krammer: private communication.

# Test Operation of Spin-Filter Polarimeter for Deuteron

I. Nishikawa, M. Watabe, and T. Tamae

*Laboratory of Nuclear Science, Tohoku University, Sendai 982-0826*

## §1. Spin-Filter Polarimeter at LNS

We have developed a Lamb-shift type polarimeter for probing the polarization of an optical pumping polarized deuteron gas target. The Lamb-shift polarimeter [1,2] is based on the 3-level interaction between $D(2S_{1/2}, \uparrow_{electron})$, $D(2S_{1/2}, \downarrow_{electron})$ and $D(2P_{1/2}, \uparrow_{electron})$ states in the spin-filter cavity. The mechanism of the 3-level interaction in the spin-filter cavity is found elsewhere [3,4]. In this report the equipment and the test operation result are described briefly. A view of the spin-filter polarimeter is shown in Fig.1.

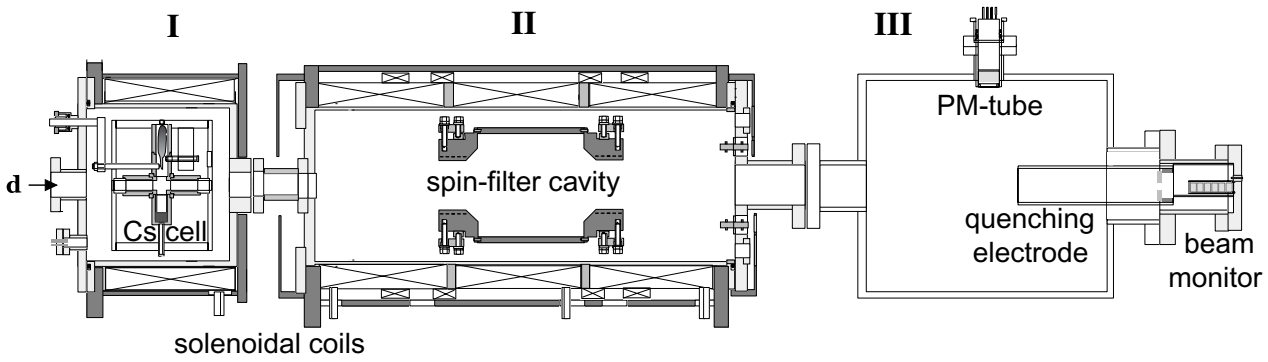


Fig.1 A view of the spin-filter polarimeter.

### 1-1 Charge Exchange Section

Some of the deuteron ions extracted from a deuterium gas target are converted to D(2S) atoms by the charge exchange reaction $d^+ + Cs \rightarrow D(2S) + Cs^+$ [5] in the Cs vapor cell. The cross-shaped Cs vapor cell is composed of inner copper sleeves and outer ceramic sleeves which are heated by a nickel-chrome ribbon heater. The cell is placed in the solenoidal coil to suppress the expected depolarization effect.

### 1-2 Spin-Filter Section

The spin filter cavity is placed in a solenoidal coil set which generates homogeneous magnetic flux in the central region of the cavity. The spin-filter coil set is composed of three main solenoidal coils of hollow conductor, two correction solenoidal coils and iron yokes. The D(2S) atoms are injected into the axial area of the cavity, and the longitudinal rf electric field and transverse static electric field quench the D(2S) atoms which are non-selected or off-resonance. The cavity is made of brass, 26cm in full-length, divided into 4-quadrant parts. It is operated at 1610 MHz in the $TM_{010}$ mode with an rf power of about 0.1 W.

### 1-3 Photon Counting Section

In this section the number of the D(2S) atoms passed the spin-filter cavity is counted. The D(2S)

atoms contained in the beam are forcedly Stark-quenched in the electric field produced by a cylindrical quenching electrode, accompanied by the emission of Lyman-alpha photons. Some of the decay Lyman-alpha photons are detected by a UV PM-tube (Hamamatsu R6835) with $MgF_2$ window, CsI cathode, and AC-coupled output. The output signals from the PM-tube are pulse-height-analysed and counted by NIM modules and a DAQ-board on PC. The typical counting rate is ~400 photons/sec in the following polarimetry operation.

## §2. Test Operation of the Polarimeter

### 2-1 RF ion injector and beam line

The test operation of the spin-filter was done by injecting unpolarized deuteron atoms from an RF-ion- source. The overview of the RF-ion-source and the ion beam optics is depicted in Fig.2.

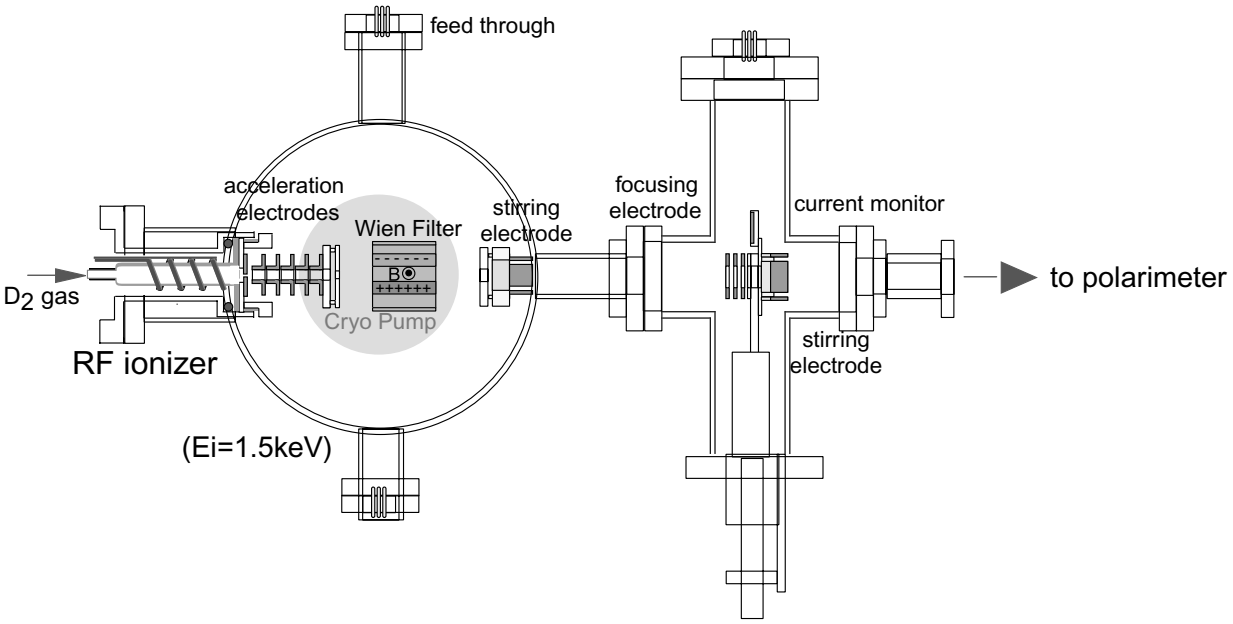


Fig.2 Test-ion injector and beam line components.

The RF ionizer is composed of a Pyrex glass tube and an RF-coil. An 13.6MHz rf power of 25W was supplied to the coil through a matching circuit. The partially-ionized and dissociated deuterium gas was ejected through a 1mm-diameter hole on a copper electrode. Ions were extracted and accelerated up to 1.5 keV by cylindrical electrodes and mass-analysed by a Wien filter. The magnetic flux (~1150 gauss at the central point) was generated by two square permanent magnets in the Wien filter. The ion beam was guided into to the Cs cell of the polarimeter by two stirring electrodes and a focusing electrode, and the beam current was measured by a beam monitor at the end of the polarimeter. A typical current of the passed ion beam was 0.3 nA at the monitor.

### 2-2 Test operation result

We measured the populations of the magnetic sub-states of unpolarized deuterons from the RF-ion source. The ion beam energy was 1.5 keV and the Cs-cell temperature was 313K. A typical result and fitted curves are shown in Fig.3. In the figiue, the averaged count rate of photons detected by the PM

tube are plotted as a function of a mean magnetic flux on the beam axis in the cavity. At each data point photon pulses were counted in 10 seconds.

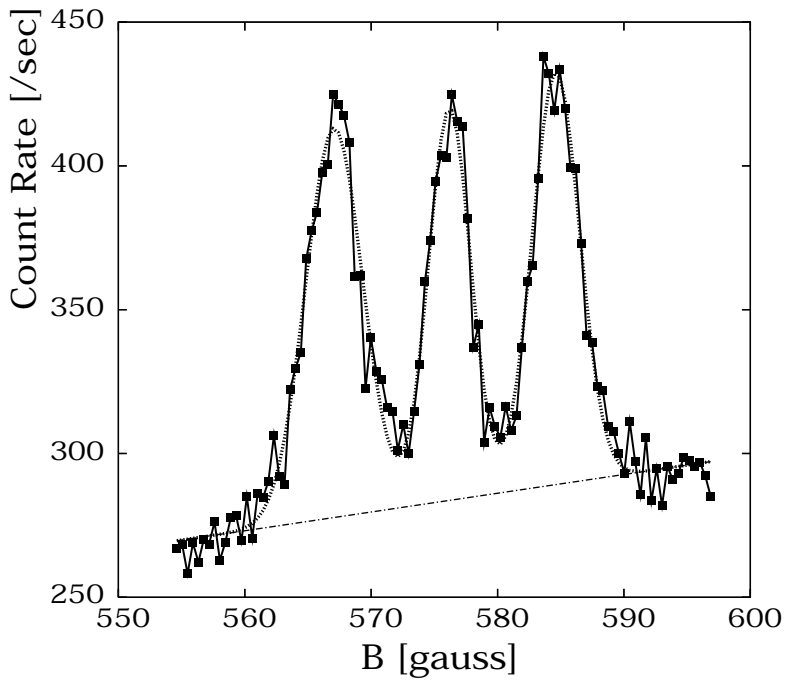


Fig.3. Observed peaks of the deuteron magnetic sub-state population:, dashed line (Gaussian + linear), dot-dashed line( a linear part of the fitting. )

In the figure the relative height of the three peaks on the straight line corresponds to the relative populations of the nuclear magnetic sub-states of the D(2S) at the quenching electric field. From the Fig.3 we note S/N and stability are not sufficient. Improvement of the homogeneity of the magnetic flux in the spin-filter region and suppression of background photons will be required.

## References

[1] J.L. McKibben and G.G. Olsen : Phys. Rev. Lett. **20** (1968) 831.

[2] S.K. Lemieux : Nucl. Instrum. and Meth. **A313** (1993) 434.

[3] G.G. Olsen and J.L. McKibben : "*Theory of a Radio Frequency "Spin Filter" for a Metastable Hydrogen, Deuterium, or Tritium Atomic Beam*" LA-3725, Los-Alamos Scientific Laboratory (1967).

[4] K. Kubo and K. Katori : *"Spin and Polarization"* Shin-Butsurigaku-Series no.27, Baifuukan-Press. (1994).

[5] P. Pradel *et al*. : Rev. Sci. Instrum. **45** (1974) 44.

# Ⅱ. Radiochemistry

(LNS Experiment : #2389, #2408, #2424, #2443, #2458, #2460, #2475, #2490, #2492, #2502, #2503, #2513, #2514, #2525, #2526, #2541, #2542)

# Observation of $\alpha$-decay of $^{229m}$Th produced from $^{229}$Ac

H. Kikunaga[1,*], Y. Kasamatsu[2], K. Takamiya[3], T. Mitsugashira[4], M. Hara[4], T. Ohtsuki[5], H. Yuki[5], A. Shinohara[2], S. Shibata[3], N. Kinoshita[1], A. Yokoyama[1], and T. Nakanishi[1]

[1]*Faculty of Science and Graduate School of Natural Science and Technology, Kanazawa University, Kanazawa 920-1192*
[2]*Graduate School of Science, Osaka University, Toyonaka, Osaka 560-0043*
[3]*Research Reactor Institute, Kyoto University, Kumatori, Osaka 590-0494*
[4]*The Oarai-branch, Institute for Materials Research, Tohoku University, Oarai-machi, Ibaraki 311-1313*
[5]*Laboratory of Nuclear Science, Graduate School of Science, Tohoku University, Sendai 982-0826*

We produced $^{229}$Th in the nuclear reaction $^{232}$Th($\gamma$, p2n)$^{229}$ Ac, followed by disintegration to $^{229m,g}$Th. The $\alpha$-decay signals from $^{229m}$Th were searched for and the alpha-particle events of the energy region between 4.93 MeV and 5.05 MeV were observed in the separated thorium fraction from an actinium source highly purified from the $^{232}$Th + $\gamma$ reaction products. The energy values of the $\alpha$-particles coincide with those expected for $^{229m}$Th.

## §1. Introduction

Recent investigations of $^{229}$Th have reported energy difference between the ground state $^{229g}$Th and the first excited state $^{229m}$Th to be (3.5 ± 1.0) eV [1, 2] or (3.4 ± 1.8) eV [3]. In those studies, $^{229m,g}$Th was produced from the $\alpha$-decay of $^{233}$U. Additional evidence for the existence of $^{229m}$Th was given by Burke *et al*. [4] using $^{230}$Th (d,t) particle reaction spectroscopy. The internal conversion process is prohibited in $^{229}$Th because the energy of the isomeric transition from $^{229m}$Th to $^{229g}$Th is lower than the first ionization potential of thorium. Therefore, the investigation of the $^{229m}$Th decay is expected to provide a strong verification of the electron bridge mechanism (EBM) [5], which is a de-excitation process competing with isomeric transition and $\alpha$-decay. Since the probability of the EBM depends on the energy state of the outer-shell electrons, the half-life of $^{229m}$Th can vary with its chemical state; hence the isomer is also interesting from a chemical viewpoint.

It is believed that no one has thus far succeeded in detecting a decay signal from $^{229m}$Th. In a few studies, the observation of photons due to isomeric or EBM transitions was attempted by ultraviolet and visible spectroscopy [6, 7], but there is still some doubt regarding the results [8, 9]. Browne *et al*. [10] searched for $^{229m}$Th from a sample prepared from approximately 25g of $^{233}$U. They tried to observe the growth of $\gamma$-rays associated with the $\alpha$-decay of $^{229g}$Th due to the feeding from $^{229m}$Th, but observed no evidence of such growth. The failure to observe these events might be attributable to two reasons: the difficulty in detecting extremely low energy photons and the small branching ratio from $^{233}$U to $^{229m}$Th,

which is about 2%.

In order to address the first difficulty, it seems reasonable to devise the identification of $^{229m}$Th by the detection of its $\alpha$-decay. The most favorable decay-mode of $^{229m}$Th should be the direct $\gamma$-transition or the EBM [5]. The observation of photon emission from the isomeric state requires detecting ultraviolet-visible photons under considerable interference, such as $\alpha$-particle induced fluorescence. Such a measurement is very difficult. On the other hand, the $\alpha$-decay of $^{229m}$Th is undoubtedly nuclear disintegration phenomenon, though as a minor decay-mode. The technique for $\alpha$-particle detection is well established and its detection is subjected to little interference from the background. Therefore, it is expected that if $\alpha$-particles from $^{229m}$Th exist, they are observable. The $\alpha$-decay of $^{229m}$Th has been discussed by Mitsugashira *et al*. [11] and Dykhne *et al*. [12]. Both expected the favored $\alpha$-particle decays from $^{229m}$Th had energies higher than those from $^{229g}$Th, i.e. 4.93-5.05 MeV. This implies that the partial half-life of the $\alpha$-decay of $^{229m}$Th is shorter than that of $^{229g}$Th.

To address the difficulty of the small branching ratio from $^{233}$U to $^{229m}$Th, we produced $^{229m}$Th from $\beta$-decay of $^{229}$Ac following a nuclear reaction process, whereas in all previous investigations on the decay properties of $^{229m}$Th, the nuclide was produced from the $\alpha$-decay of $^{233}$U. By using a suitable nuclear reaction, it was expected that the $^{229}$Th sample would have a m/g ratio large enough to observe the minor $\alpha$-decay from $^{229m}$Th, although complicated chemical procedures for eliminating by-products would be required.

Based on these ideas, we previously reported the detection of $\alpha$-decays of $^{229m}$Th produced by the $^{230}$Th($\gamma$, n) reaction [11]. Unfortunately, it appeared that the results contained interfering effects due to pile-up of the $\alpha$-particles from $^{230}$Th decay and $\beta$-rays of the other nuclear reaction products. In this reaction system, the interference was unavoidable because it is impossible to chemically separate the $^{229m}$Th from the target $^{230}$Th and other thorium isotopes produced in the reaction.

In this study, we attempted to detect the $\alpha$-decay signals from $^{229m}$Th produced using another reaction system. We obtained $^{229m}$Th from $\beta$-decay $^{229}$Ac that was produced through the reaction $^{232}$Th($\gamma$, p2n). A sample of $^{229m,g}$Th was prepared using several chemical separation methods and was measured with an $\alpha$-spectrometer.

## §2. Experimental

### 2.1 Preparation of the thorium dioxide target

A $^{232}$Th reagent, allowed to stand unprocessed for more than 40 years, contains daughter nuclei in radioactive equilibrium mixture, such as $^{228}$Ra and $^{228}$Ac. The $^{228}$Ac feeds $^{228}$Th that significantly interferes with the observation of the $\alpha$-particles of $^{229m}$Th. Therefore, $^{228}$Ra and $^{228}$Ac should be removed from thorium in radioactive equilibrium with its decay series nuclei just before bremsstrahlung irradiation. To perform such chemical separation, about 1 g of thorium dioxide was dissolved in a mixture of 10 mL of 13M (mol/dm$^3$) nitric acid ($HNO_3$) and a drop of 27M hydrofluoric acid (HF) under heating, and the solution was passed through a column packed with anion exchange resin (Dowex 1X8, 100-200 mesh, 30 mm$\phi$ × 70 mm) to adsorb thorium isotopes. The resin was washed with 150 mL of 8M $HNO_3$ to remove radium and actinium, and then thorium isotopes were eluted from the column with

150 mL of 2M HCl. A greater than 3-fold excess of saturated oxalic acid was added to the eluate under heating, then the resulting precipitate, $Th(C_2O_4)_2$, was aged for one night. The precipitate was washed with distilled water and ignited at 800 ºC for 8 hours to produce thorium dioxide.

**2.2 Bremsstrahlung irradiation**

A sample of about 1.65 g of $^{232}ThO_2$ was enclosed in a quartz tube for irradiation with bremsstrahlung radiation. The irradiation was carried out using the Electron Linear Accelerator at Tohoku University. The accelerator was operated at an electron energy of 30 MeV with a mean current of around 0.1 mA. The $^{232}ThO_2$ target was placed in close contact with the back of a platinum converter and cooled with running tap water during the 1-hour irradiation. After the irradiation, the target was chemically treated according to the procedure outlined in Fig.1 and the details given below.

**2.3 Isolation of actinium from the irradiated target**

The target material was dissolved in a mixture of 10 mL of 13M $HNO_3$ and one drop of 27M HF under heating, and diluted with water to 40 mL (diluted to about 4M $HNO_3$). In order to remove thorium isotopes from the solution, including aimed actinium, solvent extraction with 40 mL of 1M HDEHP-benzene was carried out three times in series. After washing the aqueous phase with 40 mL benzene, actinium isotopes were co-precipitated with iron hydroxide by adding 1 mg of iron and 15M ammonia water ($NH_{3aq}$). The precipitate was then dissolved in 1M $HNO_3$ and the solution passed through a cation exchange resin column (Dowex 50X8, 200-400 mesh, 5.5 mm$\phi$ × 40 mm), which adsorbs actinium isotopes. The resin was washed with 8 mL of 3M $HNO_3$ to remove radium and iron. Then actinium isotopes were eluted from the column with 12 mL of 8M $HNO_3$. The solution was passed through an anion exchange resin column (Dowex 1X8, 200-400 mesh, 5.5 mm$\phi$ × 40 mm) to completely eliminate thorium from the solution. The actinium fraction containing rare earth fission products was adjusted to a 9M HCl solution and passed twice in series through an anion- exchange resin column (Dowex 1X8, 200-400 mesh, 5.5 mm$\phi$ × 40 mm) to adsorb completely $^{231}Pa$ produced from $^{231}Th$. These purification procedures for actinium were carried out within about one hour after the end of bremsstrahlung irradiation.

**2.4 Preparation of $^{229m,g}$Th source for $\alpha$-particle counting and spectrometry**

To allow the decay of $^{229}Ac$ ($T_{1/2}$ = 62.7 min) and the growth of $^{229m,g}Th$ isotopes, the purified actinium fraction was left to stand for 3 hours after the end of the purification of actinium. The solution containing thorium isotopes was adjusted to 8M $HNO_3$ solution during these 3 hours and passed through an anion- exchange resin column (Dowex 1X8, 200-400 mesh, 5.5 mm$\phi$ × 40 mm) to adsorb the thorium isotopes. The resin was washed with 20 mL of 8M $HNO_3$ to remove rare earth fission products and actinium isotopes. The thorium isotopes were eluted from the column with 5 mL of 2M HCl and co-precipitated with samarium hydroxide by adding 30 $\mu$g of samarium and 15M $NH_{3aq}$. The precipitate was collected on a 0.02-$\mu$m alumina filter (Whatman, ANODISC membrane) of 18 mm diameter to prepare a counting source. The filter was fixed on a stainless-steel supporting ring and dried at 130 ºC. All the chemical procedures were finished about 5 hours after the end of irradiation. The sample was measured by $\alpha$-ray spectrometry with a 450 mm$^2$ silicon detector and a 2k-channel PC-PHA system. The background count rate for this detector was about 20 counts/day in the energy range of 3 to 8 MeV

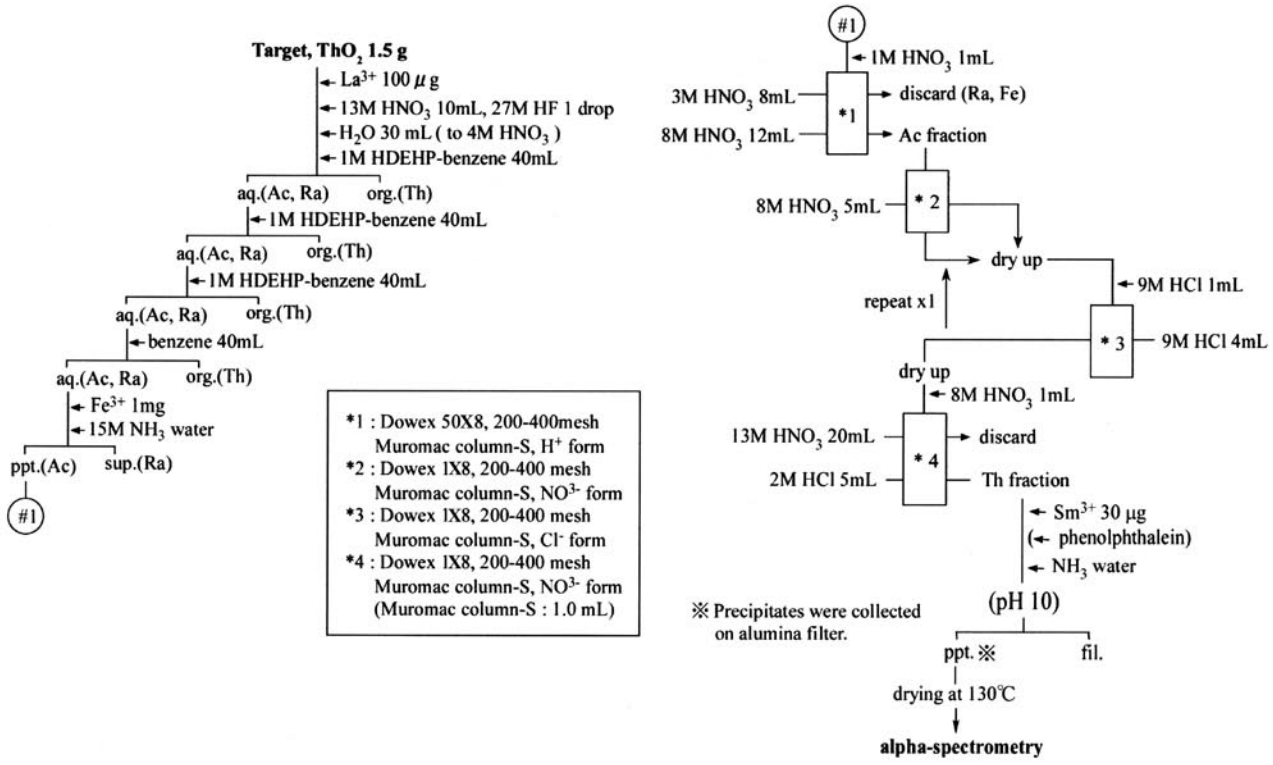


Fig.1. Chemical procedure for preparation of the $^{229m,g}$Th sample.

and less than 1 count/day in the energy range of 4.5 to 5.1 MeV. Collection of $\alpha$-events was started within 10 minutes of completing the counting source preparation and the accumulation of an $\alpha$-ray spectrum for $10^4$ -sec was repeated 90 times.

## §3. Results and discussion

An $\alpha$-ray spectrum obtained as a sum of the first 30 spectra is shown in Fig.2. The $\alpha$-peaks of $^{147}$Sm, $^{232}$Th, $^{230}$Th, and $^{228}$Th and its daughters can be observed in the spectra. Some dozen $\alpha$-counts are observed between the $^{230}$Th peaks and the $^{228}$Th peaks, at an energy consistent with that expected for $^{229m,g}$Th. It was found that the ratio of the $\alpha$-counts of $^{230}$Th/$^{229}$Th/$^{228}$Th was about 3/1/70, while it was about 5500/1/10 for the thorium sample isolated from $^{230}$Th($\gamma$, n) reaction products [11]. In this experiment, the count number of $^{230}$Th decays was relatively small and had no influence on the identification of $^{229m,g}$Th. However, interference from $^{228}$Th on the observation of $^{229}$Th may have occurred, as discussed below, because the count number of $^{228}$Th decays was greater by a factor of seven in this experiment.

A magnification of the $\alpha$-spectrum for the region related to $^{229}$Th is shown in Fig.3 (a). The spectrum of the energy region differs from the spectrum expected for only $^{229g}$Th. The causes of this difference are believed to be the peak tail from the peaks of $^{228}$Th and its daughters, $\alpha$-counts from impurities, and/or the existence of $^{229m}$Th.

$^{228}$Th was formed simultaneously with $^{229m,g}$Th by the $\beta$-decay of $^{228}$Ac produced in the $^{232}$Th($\gamma$, p3n) reaction in the source. It has the largest number of counts in the spectra and the energy region is

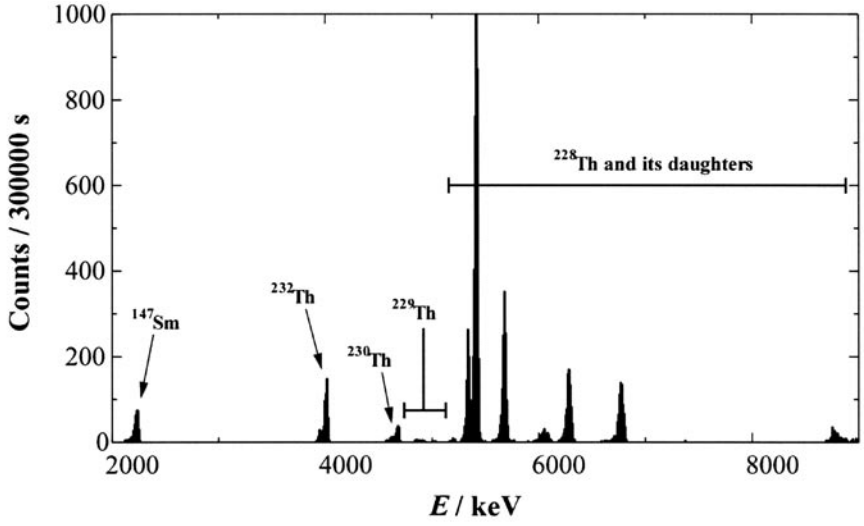


Fig.2. $\alpha$-ray spectrum acquired over a counting duration of $3 \times 10^5$ s, starting 10 minutes after the chemical separation.

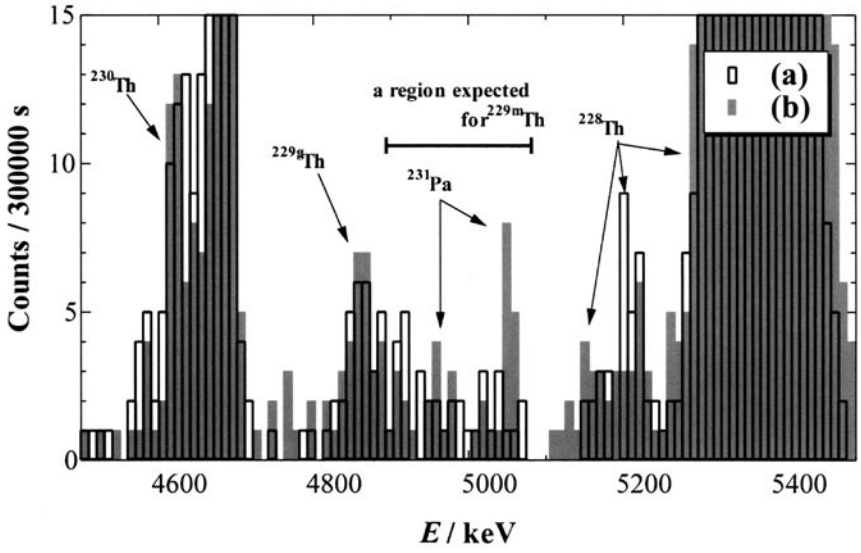


Fig.3. Expanded $\alpha$-ray spectra acquired over a counting duration of $3 \times 10^5$ s, starting 10 minutes after the chemical separation (a), and acquired 1 week after the chemical separation (b).

higher than that of $^{229m,g}$Th. It was found, however, that the high resolution spectrum is little influenced by the peak tail of $^{228}$Th. In Fig.3 (a) the $^{228}$Th peak has a FWHM of about 29 keV measured at 5423 keV.

A growth in time of the $\alpha$-count rate was observed. These counts were identified by the energy value as the $\alpha$-peaks of $^{231}$Pa. The growth of $^{231}$Pa interfered with the identification of $^{229m}$Th. The spectrum obtained one week after the chemical separation is shown in Fig.3 (b), overlaying Fig.3 (a), demonstrating the growth of $^{231}$Pa. It is thought that $^{231}$Pa was completely eliminated by the repetitive anion exchange at the end of the chemical purification of the actinium fraction and, therefore, the observed $^{231}$Pa may be the decay product of $^{231}$Th, produced in the $^{232}$Th($\gamma$, n) reaction. The counting source included $^{231}$Th because elimination of thorium was not complete. Although the decontamination

factor of thorium isotopes in the purified actinium fraction was estimated to be about $5 \times 10^{-5}$, sufficient $^{231}$Pa was produced to interfere with the identification of $^{229m}$Th because of the large cross-section of the $^{232}$Th($\gamma$, n) reaction.

The spectrum in Fig.3 (b) can be reproduced by sum of the $^{229g}$Th spectrum and the $^{231}$Pa spectrum. It indicates that the half-life of $^{229m}$Th is not as long as one week. On the other hand, the early spectrum in Fig.3 (a), before the growth of $^{231}$Pa, differs from the spectrum expected for only $^{229g}$Th. In particular the observed $\alpha$-counts between 4.93 MeV and 5.05 MeV, which coincides with the expected energy of $^{229m}$Th, were larger than those expected for $^{229g}$Th. It may be considered that the new $\alpha$-emitter $^{229m}$Th was observed in this work, although the $\alpha$-peaks are not clearly defined, probably due to poor counting statistics.

## §4. Conclusion

We attempted to produce $^{229m}$Th by the nuclear reaction $^{232}$Th($\gamma$, p2n)$^{229}$Ac, followed by disintegration to $^{229m,g}$Th. The alpha-events in the expected energy region for $^{229m,g}$Th were observed with less interference than has been achieved in previous experiments. The spectral shape differs from that expected for only $^{229g}$Th, which may be due to presence of $^{229m}$Th. A better chemical separation of actinium from thorium would eliminate the interference of $^{231}$Pa and allow more definitive results to be obtained.

## Acknowledgement

The authors are grateful to the staff in the division of accelerators of the Laboratory of Nuclear Science, Tohoku University.

## References

[1] C.W. Reich and R.G. Helmer: Phys. Rev. Lett. **64** (1990) 271.

[2] R.G. Helmer and C.W. Reich: Phys. Rev. C**49** (1994) 1845.

[3] V. Barci, G. Ardisson, G. Barci-Funel, B. Weiss, O. El Samad, and R.K. Sheline: Phys. Rev. C**68** (2003) 034329.

[4] D.G. Burke, P.E. Garrett, T. Qu, and R.A. Naumann: Phys. Rev. C**42** (1990) R499.

[5] E.V. Tkalya, A.N. Zherikhin, and V.I Zhudov: Phys. Rev. C**61** (2000) 064308.

[6] G.M. Irwin and K.H. Kim: Phys. Rev. Lett. **79** (1997) 990.

[7] D.S. Richardson, D.M.. Benton, D.E. Evans, J.A.R. Griffith, and G Tungate: Phys. Rev. Lett. **80** (1998) 3206.

[8] S.B. Utter, P. Beiersdorfer, A. Barnes, R.W. Lougheed, J.R. Crespo López-Urrutia, J.A. Becker, and M.S. Weiss: Phys. Rev. Lett. **82** (1999) 505.

[9] R.W. Shaw, J.P. Young, S.P. Cooper, and O.F. Webb: Phys. Rev. Lett. **82** (1999) 1109.

[10] E. Browne, E.B. Norman, R.D. Canaan, D.C. Glasgow, J.M. Keller, and J.P. Young: Phys. Rev. C**64** (2001) 014311.

[11] T. Mitsugashira, M. Hara, T. Ohtsuki, H. Yuki, K. Takamiya, Y. Kasamatsu, A. Shinohara, H. Kikunaga, and T. Nakanishi: J. Radioanal. Nucl. Chem. **255** (2003) 63.

[12] A.M. Dykhne, N.V. Eremin, and E.V. Tkalya: JETP Lett. **64** (1996) 345.

(LNS Experiment: #2389, #2408, #2424, #2443, #2458, #2460, #2475, #2490, #2492, #2502, #2503, #2513, #2514, #2525, #2526, #2541, #2542)

# Search for the Decay of $^{229m}$Th by Photon Detection

Y. Kasamatsu[1], H. Kikunaga[2], K. Nakashima[1], K. Takamiya[3], T. Mitsugashira[4], T. Nakanishi[2], T. Ohtsuki[5], H. Yuki[5], W. Sato[1], and A. Shinohara[1]

[1]*Graduate School of Science, Osaka University, Toyonaka, Osaka 560-0043*
[2]*Graduate School of Natural Science and Technology, Kanazawa University, Kanazawa 920-1192*
[3]*Research Reactor Institute, Kyoto University, Kumatori, Osaka 590-0494*
[4]*The Oarai-branch, Institute for Materials Research, Tohoku University, Oarai-machi, Ibaraki 311-1313*
[5]*Laboratory of Nuclear Science, Tohoku University, Sendai982-0826*

## §1. Introduction

The first excited state of thorium-229, $^{229m}$Th, is expected to show an intriguing decay property because of its extremely low-lying excitation energy. The excitation energy has been reported to be either 3.5 ± 1.0 eV or 3.4 ± 1.8 eV from the results of precise $\gamma$-ray spectroscopy conducted at the decay of $^{233}$U.

In the disintegration process from $^{229m}$Th to $^{229g}$Th, the emission of internal conversion electrons is forbidden because the disintegration energy is lower than even the first ionization energy of thorium atoms. Thus the de-excitation from $^{229m}$Th to the ground state is expected to take place through a direct $\gamma$-ray transition or decay via an electron bridge (EB) mechanism in which part of the transition energy is deposited to excite the valence-shell electrons of $^{229m}$Th. This implies that the half-life of $^{229m}$Th is directly affected by the chemical state of $^{229m}$Th.

Several experimental results have been reported by different groups about the detection of photons emitted from $^{233}$U samples that contain a considerable amount of $^{229m}$Th produced through the $\alpha$ decay from $^{233}$U with a branching ratio of about 2 %. These attempts were not successful, however, owing to interference of radiation-induced fluorescence from the materials around the radioactive $^{233}$U sample.

In our experiments, Th atoms were chemically separated by means of an anion exchange method for removing the influence of intense radiation from $^{233}$U. As for the photon detection, the detection efficiency was raised as high as possible by developing a novel detection system. In this report, the limits of the half-life of $^{229m}$Th in $HNO_3$ solution are deduced based on the experimental observations.

## §2. Experiment

Thorium-229m samples were prepared by a chemical separation from about 93mg of $^{233}$U containing 4.4 ppm of $^{232}$U by the following procedure. Uranium-233 was first sorbed in 2 cm$^3$ of an anion exchange column (Dowex 1X8, 200-400 mesh) in 9M HCl solution and its descendants except for Bi and Tl were eluted. After a given growth time, accumulated $^{229}$Th and $^{229m}$Th were eluted in 5 ml of 9M HCl solution and separated from $^{233}$U. In order to thoroughly remove $^{233}$U, the eluate was again passed through

another anion exchange column of the same resin in 9M HCl solution. We were able to accomplish the whole chemical separation within only about 3 minutes. Following the separation, 1 mg of Al and approximately 10 ml of concentrated ammonia water were added into the eluate. Thorium atoms were coprecipitated with Al in the form of hydroxide. After the decantation of the supernatant liquid, the precipitate was dissolved in 3 to 4 droplets of 8 M $HNO_3$ in order to minimize the sample volume to prepare a quasi point source. The solution sample was transferred into a small quartz bowl of a size of 6 mm in internal diameter and 10 mm in height, and photon measurements were performed.

Taking a wide range of the expected half-life of $^{229m}$Th into account, two different experiments were carried out varying the growth time: 2 and 17 hours for the first and second experiments, respectively. It took 18 minutes to accomplish the chemical separation and treatment in the first experiment, and 30 minutes in the second.

In this work, we consider that the detection efficiency precedes the energy information. Although the output signal of a photomultiplier (PM) has no information concerning the energies of incident photons, therefore, we adopted the PM designed for single photon counting. In order to improve the detection efficiency, an oval reflector was employed to focus as many photons as possible on the photocathode of the PM.

The detection efficiency was estimated taking into account several parameters: the sample geometry, the reflection efficiency of the reflector, the effect of a finite volume of the $^{229m}$Th solution sample, the quantum efficiency of the PM, and the absorbance by the $HNO_3$ solution. The whole detection efficiency was accordingly estimated to be at least $4 \times 10^{-4}$ for the photons in the range between 340 and 600 nm (3.6 - 2.1 eV).

## §3. Result and Discussion

It should be noted that $^{229m}$Th accumulates, during the growth time, depending on $T^{HCl}$, and $^{229m}$Th disintegrates, during the measurement, at the rate $T^{HNO3}$. Here, $T^{HCl}$ and $T^{HNO3}$ denote the half-lives of $^{229m}$Th as a solute in HCl and $HNO_3$ solutions, respectively. Since the chemical condition of $^{229m}$Th turns during the preparation of the sample, the following discussion on $T^{HNO3}$ is based on the number of $^{229m}$Th atoms grown in the HCl solution.

In Fig. 1 and 2 are shown the time variation of the photon counting rate for the first experiment (2-hour growth time) and that for the second experiment (17-hour growth time), respectively. The horizontal dashed lines represent the constant background level obtained by a blank measurement. It is obvious from the figures that additional photons deriving from the $^{229m}$Th source as well as from the other descendants were not evidently detected.

Although the half-life cannot be determined, the limits of the half-life can be estimated from the results. The estimation of the limit of $T^{HNO3}$ requires 1) the lower limit of the number of $^{229m}$Th atoms at the end of the growth in the HCl solution and 2) the detection efficiency which has already been estimated. The number of $^{229m}$Th atoms can be figured from the activity of $^{229m}$Th at the end of the growth time. If $T^{HCl}$ is 3 minutes, which was taken for the chemical separation, or shorter, it would be difficult to estimate the limit of $T^{HNO3}$ because of their decay loss during the separation. From these

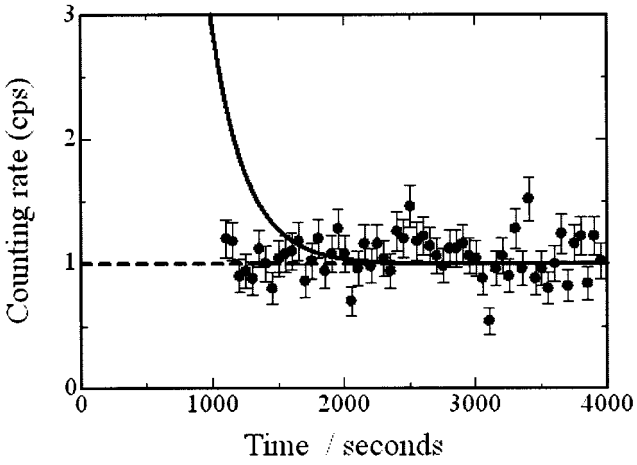


Fig.1. Time variation of the counting rate for photons emitted from $^{229m}$Th $HNO_3$ solution sample grown for 2 hours in the 9M HCl.

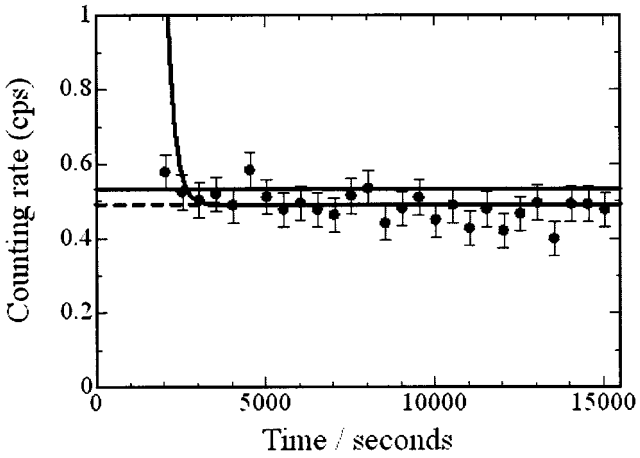


Fig.2. Time variation of the counting rate for photons emitted from $^{229m}$Th $HNO_3$ solution sample grown for 17 hours in the 9M HCl.

conditions, the limits were estimated as follows.

1) If $T^{HCl}$ is shorter than 3 minutes, it is difficult by the present experimental method to observe evident photon events for any half-life of $^{229m}$Th in $HNO_3$ solution.
2) If $T^{HCl}$ is longer than 3 minutes, $T^{HNO3}$ can be limited as $<$ 3 minutes or $>$ 60 hours as indicated by solid line in Fig. 1. Especially referring to the case that $T^{HCl}$ is longer than 3 hours, the number of $^{229m}$Th atoms accumulated during the growth time is almost constant in both experiments and

$T^{HNO3}$ should be $< 2$ minutes or $> 400$ days as indicated by the solid lines in Fig. 2.

For further discussion about $T^{HNO3}$, more detailed information on $T^{HCl}$ is necessary. A new device for the preparation of a point source of $^{229m}$Th is now under development.

(LNS Experiment : #2427, #2442, #2457, #2474, #2489, #2499, #2512, #2524)

# Life-time measurement of $^{7}$Be in beryllium metal

T. Ohtsuki[1], Y. Yuki[1], M. Muto[1], J. Kasagi[1], K. Ohno[2]

[1]*Laboratory of Nuclear Science, Tohoku University, Mikamine, Taihaku, Sendai 982-0826*
[2]*Department of Physics, Yokohama National University, 79-5 Tokiwadai, Hodogaya, Yokohama 240-8501*

The decay rate of $^{7}$Be (nucleus of electron-capture decay) was measured in Be metal. The half life of $^{7}$Be in Be metal (Be metal ($^{7}$Be)) is found to be 53.12 ± 0.05 days. We have found that the decay rate of $^{7}$Be in Be metal is almost corresponding to that in graphite host, Lithium fluoride host etc. reported within the errors.

## §1. Introduction

As first suggested by Segré *et al*. [1-4], electron-capture (EC) decay rates depend on the density of atomic electrons within the nucleus. Environment factors such as chemical form, pressure, etc. may alter the electron contact densities at nucleus, and thus, affect the electron-capture decay rates. Here, the nucleus $^{7}$Be is a good candidate in which to look for such variations in environmental factors because of its simplest electronic structure, $1s^2 2s^2$, in the EC decay nucleus. The $^{7}$Be decays directly to the $3/2^-$ ground state of $^{7}$Li with a branching of 89.6 %, and goes to the first excited state in $^{7}$Li ($1/2^-$ at 478 keV) with that of 10.4 %, which decays by $\gamma$ emission to the ground state [5-7]. In recent research, there have been several reports of variations as a function of the host metals [8-12] and chemical forms [13-15] and pressure [16-17]. Although, a precise measurement may be still needed to obtain the absolute decay rate in the different circumstances [18-21].

Because of the uniform lattice structure (*hcp*) including $^{7}$Be in Be metal, the electron contact density on $^{7}$Be nucleus should be essentially surveyed. In the present study, we have measured the half-life of $^{7}$Be in Be metal by using a standard clock time.

## §2. Experimental procedure

Be metal (*hcp* lattice structure) of 10 mm (in diameter) × 0.3 mm (in thickness) was utilized to produce $^{7}$Be uniformly in the metal. After being washed with HCl solution, the Be metal was sealed in a quartz tube (vacuum packing) of 12 mm in diameter as a target. The irradiation with a bremsstrahlung (50 MeV electrons) was carried out at the Electron Linear Accelerator, Laboratory of Nuclear Science, Tohoku University. The sample in a quartz tube was set in the middle of a sweep magnet placed on the axis of the electron beam. A platinum converter in 2 mm thickness was set in front of the sweep magnet to generate a bremsstrahlung. Then, the sample was irradiated only by the bremsstrahlung (all electrons were ruled out by the magnetic field). Therefore, the damage to a lattice of Be metal was confined to the minimum. The experimental setup for irradiation is shown in Fig.1. The $^{7}$Be can be

produced uniformly by the $^{9}Be(\gamma, 2n)\ ^{7}Be$ reaction in the Be metal. After irradiation, the sample was baked in an electric oven of vacuum packing at 1100 ºC (a melting point of Be metal: 1278 ºC) for 1 hour to recover the lattice defect even if the lattice defect occurs by the $(\gamma, 2n)$ reaction. Finally, the sample was washed again with HCl solution to clean up the surface.

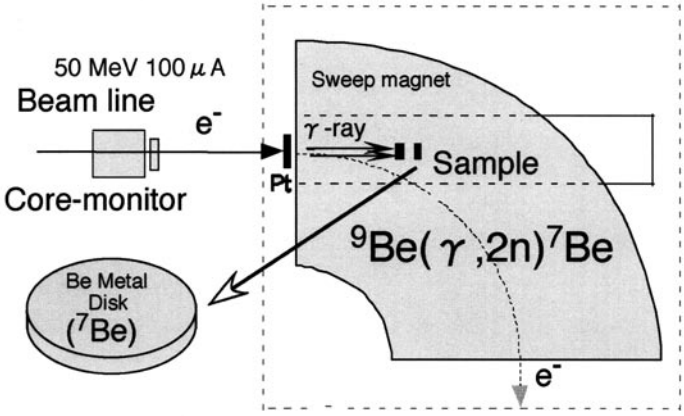


Fig.1. Setup for irradiation of Be metal.

The two samples of Be metal($^{7}Be$) and $^{7}Be@C_{60}$ for reference of the sample were placed in an automated sample changer, which horizontally moved the samples in front of a $\gamma$-ray detector. This allowed the decay rates of the two samples to be measured in a comparable way. The system is shown in Fig.2. The activities of the $^{7}Be$, the 478 keV $\gamma$-rays emanating from $^{7}Be$, was measured with a high-purity germanium (HPGe) detector ($\Delta E_{FWHM}$ is 1.8 keV and 50 % relative efficiency) coupled to a 2048-channel pulse-height analyzer. Due to the excellent energy resolution of the HPGe detector, a good

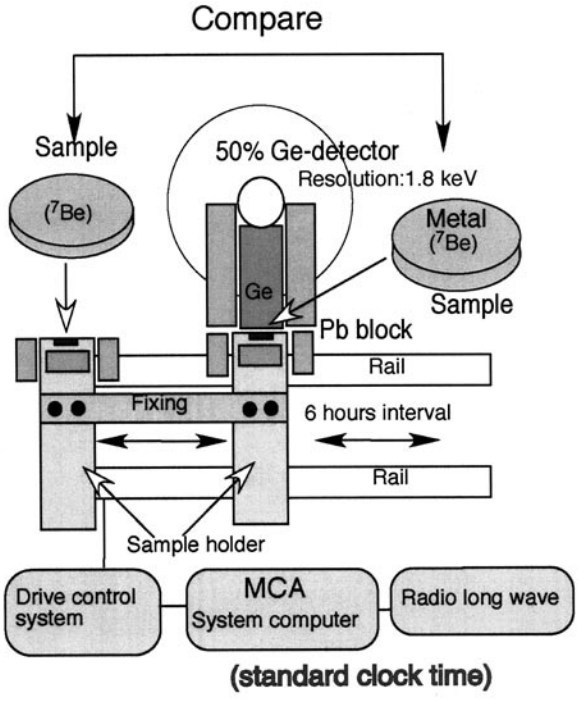


Fig.2. Experimental setup.

signal-to-noise ratio was obtained. The background was reduced by a lead shield. Therefore, the background peaks do not impair the determination of the half-life of $^{7}$Be in the present experiment. The radioactivities of $^{7}$Be could be uniquely detected by means of its characteristic $\gamma$-rays, and any other sources were ruled out. We measured 330 points with durations of $T_d \sim 6$ hours. Total measuring time was now 170 days that was over three half-lives of $^{7}$Be. The start time for each run was taken from a time standard signal distributed via a long-wave radio center in Japan. Therefore, the uncertainty in time measurements can be neglected.

## §3. Results and discussion

A typical $\gamma$-ray spectrum obtained in the sample of Be metal ($^{7}$Be) is shown in Fig.3. The expected $\gamma$ line at $E_\gamma = 478$ keV and a natural background line at $E_\gamma = 1461$ keV can be seen as two giant peaks. No peaks were seen at around $E_\gamma = 478$ keV when the $^{7}$Be sources was absent. In Fig.4, the exponential decay curve of the $^{7}$Be activities for sample of Be metal ($^{7}$Be) is shown as a function of the time (days). The decay curve obtained in the present measurement was fitted including the statistical errors by a Minuit program distributed from the CERN Program Library. The statistical error is dominating the uncertainty in each data point in Fig.4. The uncertainty of our measurement is given by the uncertainty of the slope of the straight line fitted to the logarithm of the counts (*i.e.* counts per second) of the decay spectrum. The result for the sample Be metal ($^{7}$Be) is $T_{1/2} = 53.12 \pm 0.05$ days. The dead time in the data acquisition system is evaluated to be about 8 ~ 9 sec to the each running time. Therefore, the uncertainty due to the dead time is estimated to be almost 0.04 % and this value is smaller than the fitting errors of the half-life of $^{7}$Be. The counting rates of the natural background, which is the 1461 keV $\gamma$-rays emanating from $^{40}$K, is also shown in Fig.4. The data for $^{40}$K obtained was also fitted with

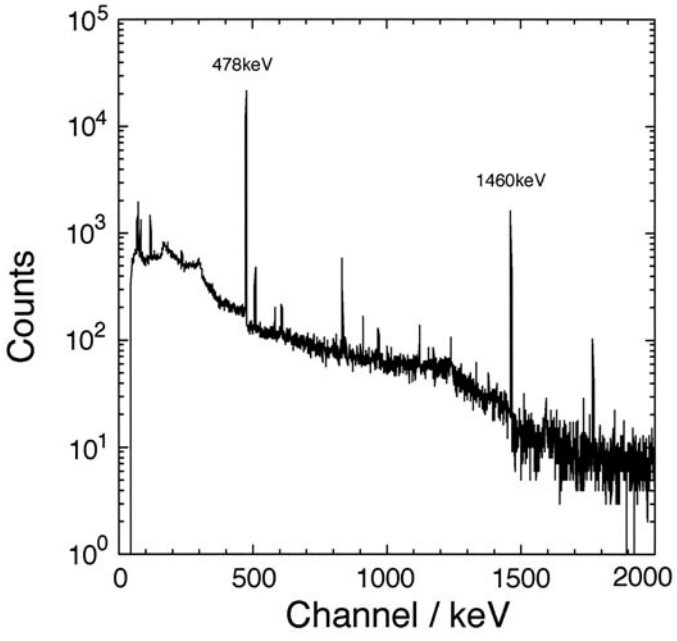


Fig.3. Typical $\gamma$-ray spectrum of the $^{7}$Be in the sample of Be metal.

the same procedures. It was found that the fitted line is corresponding to a horizontal one. (It should be noted that we have also measured the half-life of $^{7}$Be in the sample of $^{7}$Be@$C_{60}$. The result have been presented in another paper [22])

The half-life obtained in the sample of Be metal ($^{7}$Be), $T_{1/2}$ = 53.17 ± 0.05 days, is almost corresponding to the data, LiF ($^{7}$Be) and graphite etc., which is reported by Jaeger *et al.* and Norman *et al.* [8, 11], in which, the start time for each run were taken from the time standard signal distributed publicly. Further, the half-life of $^{7}$Be in several host materials (Graphite, Boron nitride etc.) has been summarized by Notrman *et al.* [11]. The value ($T_{1/2}$) is almost with in 53.1 ~ 53.3 days as shown in Table 1. Therefore, we found that the variation ($T_{1/2}$) of $^{7}$Be for Be metal ($^{7}$Be) almost corresponds to the data presented so far.

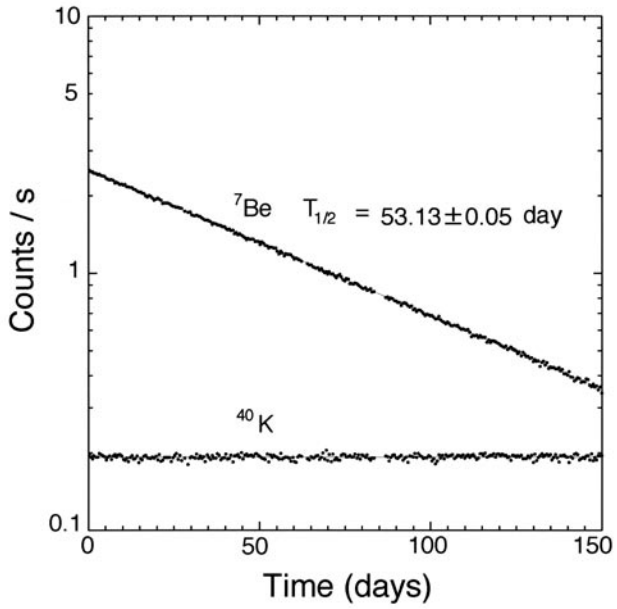


Fig.4. Exponential decay line of $^{7}$Be in the sample of Be metal ($^{7}$Be). Background radioactivities of $^{40}$K are also shown in the figure.

Table 1. Half-life of $^{7}$Be in Be Metal as determined with a least-squared fit. Half-lives previously measured are also shown as a comparison.

| Host material | $T_{1/2}$ | Ref. No. |
|---|---|---|
| Beryllium | 53.12 ± 0.05 | This work |
| Lithium fluoride | 53.12 ± 0.07 | 8) |
| Graphite | 53.107 ± 0.022 | 11) |
| Boron niteride | 53.174 ± 0.037 | 11) |
| Tantalum | 53.195 ± 0.052 | 11) |
| Gold | 53.311 ± 0.042 | 11) |
| Aluminum | 53.17 ± 0.02 | 15) |

## §4. Conclusion

We have measured the half-life of $^{7}$Be which is produced in Be metal using a HPGe detector taking into account a standard time. We found that the half-life of $^{7}$Be in Be metal was $T_{1/2} = 53.12 \pm 0.05$ days.

## Acknowledgments

The authors are grateful to the technical staff of the Laboratory of the Nuclear Science, Tohoku University for beam-handling.

## References

[1] E. Segré: Phys. Rev. **71** (1947) 274.

[2] R. Daudel: Rev. Sci. **85** (1947) 162.

[3] E. Segré and C.E. Wiegand: Phys. Rev. **75** (1949) 39.

[4] R.F. Leininger, E. Segré, and C. Wiegand: Phys. Rev. **76** (1949) 897.

[5] R.B. Firestone, V.S. Shirley, C.M. Baglin, S.Y. Frank Chu, J. Zipkin, C. M. Lederer, and V. S. Shirley: Eds. *Table of Isotopes*, 8th Ed. Vol.I (John Wiley & Sons, Inc., 1996).

[6] Ajzenberg-Selove: Nucl. Phys. A**490** (1988) 1.

[7] G.T. Emery: Ann. Rev. Nucl. Sci. **22** (1972) 165.

[8] M. Jaeger, S. Wilmes, V. Kölle, G. Staudt, and P. Mohr: Phys. Rev. C**54** (1996) 423.

[9] A. Ray, P. Das, S.K. Saha, S.K. Das, B. Sethi, A. Mookerjee, C. Basu Chaudhuri, and G. Pari: Phys. Lett. B**455** (1999) 69.

[10] A. Ray, P. Das, S.K. Saha, and S.K. Das: Phys. Lett. B**531** (2002) 187.

[11] E.B. Norman, G.A. Rech, E. Browne, R.M. Larimer, M.R. Dragowsky, Y.D. Chan., M.C.P. Isaac, R.J. McDonald, A.R. Smith: Phys. Lett. B**519** (2001) 15.

[12] Z.Y. Liu, C.B. Li, S.G. Wang, J. Zhou, Q.Y. Meng, S.J. Lu, and S.H. Zhou: Chinese Phys. Lett. **20** (2003) 829.

[13] C.A. Huh: Earth and Planetary Sci. Lett. **171** (1999) 325.

[14] H.W. Jphlige, D.C. Aumann, and H.J. Born: Phys. Rev C**2** (1970) 1616.

[15] F. Lagoutine, J. Legrand, and C. Bac: J. Appl. Radiat. Isot. **26** (1975) 131.

[16] W.K. Hensley, W.A. Bassett, and J.R. Huizenga: Science **181** (1973) 1164.

[17] L. Liu and C.A. Huh: Earth and Planetary Sci. Lett. **180** (2000) 163.

[18] The half-life of $^{7}$Be in the different chemical forms has been measured in several experiments. It should be noted that: Huh [13] has reported the half-life of $^{7}$Be in the different chemical forms, $Be^{2+}(OH_2)_4$, Be $(OH)_2$, and BeO, and they claimed that the observed difference is as much as 1.5% (in Ref. 13). In early study, Johlige [14] *et al.* have reported the half-life of $^{7}$Be in similar chemical forms ($Be^{2+}$ $(OH_2)_4$, BeO, etc.) and the variations were only within around 0.1%.

[19] A. Ray, P. Das, S.K. Saha, and S.K. Das: Science **287** (2000) 1203.

[20] H. Geissel and G. Münzenberg: Eur. Phys. J. A**13** (2002) 247: The half-life of $^{7}$Be depends on the plasma density in the vicinity of the $^{7}$Be nucleus. This value can be determined in experiments on

[7]Be in different charge states which are planned at GSI.

[21] J.A. Tossel: Earth and Planetary Sci. Lett. **195** (2002) 131.

[22] T. Ohtsuki, H. Yuki, M. Muto, J. Kasagi, and K. Ohno: Phys. Rev. Lett. **93** (2004) 112501.

(LNS Experiment：#2523, #2539)

# 光量子放射化分析法による$KTa_{1-x}Nb_xO_3$単結晶中の不純物分析

鹿野弘二[1]，大槻　勤[2]，結城秀之[2]，藤浦和夫[3]，笹浦正弘[3]

[1]函館工業高等専門学校（042-8501　函館市戸倉町14番1号）
[2]東北大学理学部付属核理学研究施設（982-0826　仙台市太白区三神峯1-12-1）
[3]NTTフォトニクス研究所（243-0198　厚木市森の里若宮3-1）

# Photon Activation Analysis of Impurities in $KTa_{1-x}NbxO_3$ Single Crystals

K.Shikano[1], T.Ohtsuki[2], H.Yuki[2], K.Fujiura[3], M.Sasaura[3]

[1]*Hakodate National College Technology, Tokura-cho 14-1, Hakodate, Hokkaido 042-8501*
[2]*Laboratory of Nuclear Science, Tohoku University, Mikamine, Taihaku-ku, Sendai, Miyagi, 982-0826*
[3] *NTT Photonics Laboratories, Nippon Telegraph and Telephone Corporation, Morinosato, Atsugi, Kanagawa, 243-0198*

The determination of Fe, Co, Ni, Cu, and Pt in $KTa_{1-x}NbxO_3$ single crystals for opto-electronics devices has been studied by using photon activation analysis. With this approach it was difficult to determine these impurities non-destructively because of the large activity of nuclides with long half-lives such as $^{182}$Ta and $^{92m}$Nb produced from matrices. Therefore, chemical separation was studied to remove such nuclear interferents as $^{182}$Ta and $^{92m}$Nb. $^{92m}$Nb and $^{58}$Co were used as tracers. It was found that $^{58}$Co could be separated by the extraction with TPB and by the anion exchange.

$KTa_{1-x}NbxO_3$（KTN）結晶中の不純物（Fe，Co，Ni，Pt）の光量子放射化分析法を検討した。その結果，マトリックから半減期が115dの$^{182}$Taと10.2dの$^{92m}$Nbが生成し，これらの生成放射能が大きいことから非破壊分析が不可能であることが分かった。そこで，$^{92m}$Nbと$^{58}$Coをトレーサにして TPBによる溶媒抽出，陰イオン交換体による分離を試みた結果，Coのみを分離できる条件を明らかにした。

## §1．はじめに

通信容量の増大にともないネットワークの大容量化・高機能化を目的とした光部品の小型化，省電力化，高機能化の開発がすすめられている。$KTa_{1-x}NbxO_3$（KTN）結晶は世界最高の電気光学効果を有し，光変調器や光スイッチなどの従来の$LiNbO_3$光デバイスの駆動電圧やサイズを一桁改善できると共に，次世代の高機能デバイス期待されている[1]。一方，材料開発において材料特性を向上する方法の一つとして，材料中の不純物濃度を明らかにし，材料作製条件を改善することにより純度を高める高純度化があげられる。半導体，光ファイバなどの通信用材料も高純度化により材料特性が向上し，今日の光通信技術が確立されてき

た。KTN結晶についても同様であり，さらなる光学特性の向上には，高純度化が不可欠であり，したがって結晶中の不純物評価が重要な課題である。

本研究では，光量子放射化分析法により，KTN結晶中の不純物を定量し，材料特性との相関を明らかにする。目的元素として，製造過程で汚染が予想されるFe，Co，Ni，Ptの定量を進める。まず，①マトリックから生成する放射性元素を明らかにするとともに放射能強度を測定し，非破壊分析の可能性を検討する。②比較標準試料を照射し，検出限界値を明らかにする。③化学分離法の開発のため，トレーサ実験を行う。試料溶解法を検討する。

## §2．実　　験

### 2.1　試　　料

分析試料に用いたKTN結晶はNTTフォトニクス研究所で作製された［1］。サイズは約10×10mm²で厚さは約0.5mmである。比較のため，NTTフォトニクス研究所で作製された$KTaO_3$（KT）結晶も使用した。これらの結晶を約5×5mm²に切断後，塩酸水溶液，蒸留水，アルコールにより超音波洗浄し，照射試料とした。また，標準試料には，市販のFe，Co，Ni，Pt箔を使用し，分析試料と同様に約5×5mm²に切断し，照射試料とした。また，フラックスモニターには市販のCu箔を使用した。

### 2.2　照射と測定

光量子照射は東北大学理学部付属核理学研究施設の電子線ライナックにより行った。KTN結晶とKT結晶を$HF-HNO_3$系のエッチング液と蒸留水により超音波洗浄した後，フラックスモニターのCu箔とともにアルミニウム箔に包み，30MeV，100 $\mu$Aの条件で20min，1hr，8hrの条件で照射した。照射後，表面汚染を除去するため$HF-HNO_3$系のエッチング液と蒸留水により超音波洗浄した後，Ge検出器－4096ch波高分析装置により放射能測定を行った。また，標準試料として，Fe，Co，Ni，Pt箔を分析試料と同様の方法で照射した。

### 2.3　化学分離

照射後，表面汚染を除去した分析試料を$Na_2CO_3$とともに白金るつぼ中で溶融した。得られた溶融物は温水，$HNO_3$で溶解し，テフロン蒸発皿上で蒸発乾固した。これにHF溶液を加え，イオン交換分離，溶媒抽出に用いた。これら分離法の分配係数はこれまで多く報告されている。ここでは，HF系溶液による陰イオン交換分離［2］ならびにHF-HCl系溶液／TPBによる溶媒抽出［3, 4］を採用することとし，以下の操作で分離を行った。

陰イオン交換体としてDowex1-8（50-100mesh）の約5 gを文献［5］にしたがい洗浄後，カラムに挿入し，1MHF溶液を流して前処理した。このカラムに分析試料溶液を加え，1Mフッ酸溶液を0.3ml/minの速度で流し，溶離液の放射能をGe検出器－4096ch波高分析装置により測定した。

溶媒抽出は以下のように行った。蒸発乾固物を7MHF－5MHCl溶液に溶解後，TPB溶液とともに30分振とうした。有機相，水相の一定量を分取し，Ge検出器－4096ch波高分析装置により放射能測定した。

## §3．結果と考察

### 3.1　非破壊分析の可能性

標準試料のFe，Co，Ni，Ptから（$\gamma$, n）反応により$^{58}$Co，$^{57}$Ni，$^{191}$Pt，$^{195m}$Ptが，また，（n, $\gamma$），（$\gamma$,

第１表　Nuclear reaction of Fe, Co, Ni, Pt and nuclear interference produced by the matrix by Bremsstrahlung bombardment

| Nuclear reaction | Half-lufe | Decay mode | $E_\gamma$, keV (%) |
|---|---|---|---|
| $^{54}$Fe ($\gamma$, 2n) $^{52}$Mn | 5.6d | EC, $\beta^+$, | 1434.1 (100) |
| $^{57}$Mn ($\gamma$, p) $^{56}$Mn | 2.6h | $\beta^-$ | 846.8 (98.9) |
| $^{59}$Co ($\gamma$, n) $^{58}$Co | 70.8d | EC, $\beta^+$ | 810.8 (99.4) |
| $^{59}$Co ($\gamma$, 2n) $^{57}$Co | 78.8d | EC, $\beta^+$ | 846.8 (99.9), 1238.3 (67.0) |
| $^{58}$Ni ($\gamma$, n) $^{57}$Ni | 35.9h | EC, $\beta^+$ | 1377.6 (77.6) |
| $^{58}$Ni ($\gamma$, 2n) $^{56}$Ni | 6.1d | EC | 811.9 (74.1) |
| $^{192}$Pt ($\gamma$, n) $^{191}$Pt | 2.8d | EC | 538.9 (13.7) |
| $^{196}$Pt ($\gamma$, n) $^{195m}$Pt | 4.0d | IT | 129.7 (2.81) |
| $^{41}$K (n, $\gamma$) $^{42}$K | 12.4h | $\beta^-$ | 1524.7 (17.9) |
| $^{181}$Ta (n, $\gamma$) $^{182}$Ta | 115d | $\beta^-$ | 1121.3 (35.0), 1189.1 (16.5), 1221.4 (27.4) |
| $^{181}$Ta ($\gamma$, n) $^{180m}$Ta | 8.1h | EC, $\beta^-$ | 103.4 (0.6), 500.7 (12.8) |
| → $^{180m}$Hf | 5.5h | IT | 215.3 (81.7), 332.3 (94.4), 443.2 (85.3) |
| $^{180}$Ta ($\gamma$, 2n) $^{178B}$Ta | 2.4h | EC | 331.7 (31.8) |
| → $^{178m1}$Hf | 4.0s | IT | 213.4 (82.4), 325.6 (94.1), 426.4 (97.0) |
| $^{93}$Nb ($\gamma$, n) $^{92}$Nb | 10.2d | EC, $\beta^+$ | 912.8 (1.7), 934.5 (99.2), 1847.3 (0.9) |

2n）および（$\gamma$, p）反応により$^{52}$Mn，$^{56}$Mn，$^{57}$Co，$^{56}$Ni，が生成することがわかった。これらの核種の核データを第１表に示す。第１表に示したように，$^{56}$Mnの放出する$\gamma$線のエネルギーは846.8keVで$^{57}$Coからの$\gamma$線と同じであり，共存すると互いに妨害となり得る。しかし，半減期が2.58hrと短いため，照射後数日冷却することにより妨害は除去できる。

一方，マトリックからの妨害を検討するため，KTN結晶とKT結晶の$\gamma$線照射を行った。その結果，KT結晶からは，（n, $\gamma$）反応により$^{42}$K，$^{182}$Taが，（$\gamma$, n）反応により$^{180m}$Ta，$^{178B}$Taが，また，その壊変核種である$^{180m}$Hfと$^{178m1}$Hfが生成することがわかった。また，600keV以上の$\gamma$線領域では生成放射能が比較的小さいことがわかる。一方，KTN結晶ではこれらの核種に加え，（$\gamma$, n）反応により$^{92m}$Nbが生成することがわかった。また，700keV以下の領域では，$^{92m}$Nbからの934keVの$\gamma$線によるコンプトン散乱によりバックグランドが増大し，放射能測定の妨害となることがわかった。これら核種の核データも第１表に示す。

以上の結果から，マトリックから生成する半減期115dの$^{181}$Taと10.2dの$^{92m}$Nbが放射能測定の妨害核種といえる。これに対して，Fe，Co，Ni，Ptから生成した半減期が約1.5dから約300dまでの核種を目的核種として，長時間照射して数日冷却後，放射能測定することにより，非破壊分析が可能と推測された。そこで，以下の検討を行った。

KT結晶およびKTN結晶の100～200mgを8hr照射し，表面汚染を化学エッチングにより除去した後，１週間冷却した。これを約１週間ごとに30000秒測定し，$\gamma$線スペクトルの変化を調べるとともに，$^{52}$Mn，$^{58}$Co，$^{57}$Co，$^{57}$Ni，$^{56}$Ni，$^{19}$1Pt，$^{195}$mPtについて測定可能かどうかもあわせて調べ，非破壊分析の可能性を検討した。第１図，第２図に照射から１週間後，３週間後，５週間後のKT結晶およびKTN結晶からの$\gamma$線スペクトルを示す。第１図と第２図から，KT結晶では200～500keVにおける$\gamma$線は１週間以上冷却することで減衰することがわかった。一方，1000keV以下の領域で$^{182}$Taの1121～1221keVの$\gamma$線によるコンプトン散乱の影響が生じ，測定の妨害になることがわかった。これに対し，KTN結晶では，Nbが入ることにより生成放射能が$\gamma$線エネルギー全体で一桁以上増加すること，５週間の冷却により約一桁減少することがわかる。これは，$^{92m}$Nbの半減期が10.2dであることから，$^{92m}$Nbの影響が約一桁減少したことによる。

以上の結果から，マトリックスの放射能強度が１ヶ月の冷却後でも大きく，非破壊分析は困難であると結

論した。そこで，化学分離法による定量を検討した。

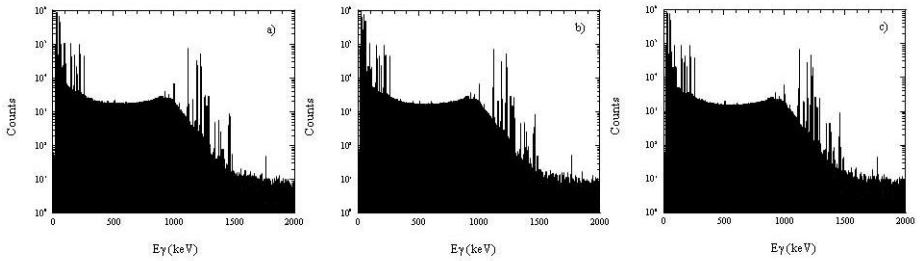


Fig.1. $\gamma$ -ray spectra of $KTaO_3$ single crystal. Cooling for a) about 1 week, b) 3.4 weeks and c) 5.4 weeks after irradiation.

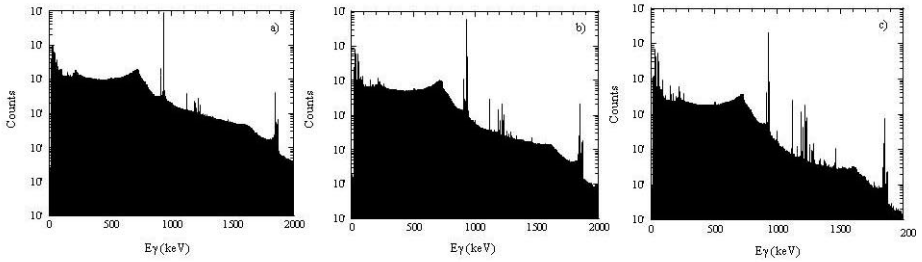


Fig.2. $\gamma$ -ray spectra of $KTa_{1-x}NbxO_3$ single crystal. Cooling for a) 1.4 weeks, b) 3 weeks and c) 5.1 weeks after irradiation.

### 3.2 化学分離法の検討

#### 3.2.1 溶解法の検討

化学分離を行うには，試料の迅速溶解が必要である。KT結晶，KTN結晶いずれも無機酸に溶解しにくいことは知られている。そこで，$Na_2CO_3$によるアルカリ溶融を検討した。ここでは，KTN結晶について検討した結果を示す。約80mgのKTN結晶を$Na_2CO_3$0.5g，1g，1.5g，2gにより白金るつぼ中で加熱，溶融し，溶融時間を調べた。その結果，$Na_2CO_3$ 2gを用いることにより，約２時間でほぼ溶融することがわかった。その後，温水と硝酸により溶融物を溶解した。

#### 3.2.2 イオン交換法の検討

３.１の結果から，$^{181}$Ta，$^{92m}$Nbから$^{52}$Mn，$^{58}$Co，$^{57}$Co，$^{57}$Ni，$^{56}$Ni，$^{191}$Pt，$^{195m}$Ptを分離する必要がある。そこで，30分間照射したKTN結晶を用いて分離条件を検討することとした。その結果，アルカリ溶融物を温水と$HNO_3$により溶解後，蒸発乾固したところ透明の結晶が析出した。これは，$NaNO_3$が析出したと思われた。これに1MHF 2mlを加えた後析出物を遠心分離し，沈殿物と上澄み液の放射能を測定した。その結果，マトリックス中の$^{92m}$Nbのうち，約60％が沈殿物に含まれ，約40％が上澄み液に残留することがわかった。この上澄み液を再度蒸発乾固したところ，再度透明の結晶が析出した。これに1MHF約2mlを加えて析出した結晶を溶解後，前処理した陰イオン交換体のカラムに注入，1MHF溶離液を0.3ml/minの速度で流し，溶離液の放射能を測定した。その結果，はじめの３フラクションまでは何も検出されず，第４フラクション目から$^{92m}$Nbが測定された。このことから，KTN結晶中の不純物濃度が低く，照射時間が30分程度では検出できないこと，また，上澄み液中の$^{92m}$Nbの放射能が大きいため比較的早めに溶離し測定の妨害になり得ることがわかった。そこで，イオン交換分離の前にTPB溶媒抽出による$^{92m}$Nbの除去を検討した。

### 3.2.3　溶媒抽出による$^{92m}$Nbの除去

3.2.1と同様に，照射したKTN結晶の溶融，溶融物の溶解，蒸発乾固，析出結晶の遠心分離を行った後，上澄み液を再度蒸発乾固し，7MHF－5MHCl溶液を6ml加えて析出結晶を溶解した。この溶液にTPB 15ml加え，15分振とうした。遠心分離後，水相，有機相の放射能を測定した。その結果，$^{92m}$Nbの約90％がTPBにより抽出され，水相の$^{92m}$Nbが1/10まで除去できることがわかった。

### 3.2.4　Coの分離

続いて，$^{58}$Coと$^{92m}$Nbをトレーサに用い，溶媒抽出とイオン交換分離を組み合わせた分離操作でCoが化学分離できることを確認する実験を行った。

3.2.3と同様に，照射したKTN結晶の溶融，溶融物の溶解，蒸発乾固，析出結晶の遠心分離を行った後，上澄み液に$HNO_3$を加え，別に照射したCo箔（13.61mg）を入れ，溶解した。溶解液を蒸発乾固した後，TBP溶媒抽出をおこなった。水相を蒸発乾固した後，1MHF溶液とし，3.2.2と同様にしてイオン交換分離を行った。第３図に，溶離液フラクション毎の$^{58}$Coと$^{92m}$Nbの放射能強度の変化を示した。図に示したように，第１から第５フラクションまで１％から最大50％まで$^{58}$Coが溶離した。第１から第５フラクションまでの$^{58}$Co放射能の合計から，Coが溶媒抽出とイオン交換を組み合わせた分離操作によりほぼ100％溶離し，損失のないことが分かった。一方，$^{92m}$Nbはいずれものフラクションにおいても検出限界以下であった。以上のことから，TBP溶媒抽出とイオン交換分離を組み合わせた分離操作により$^{92m}$Nbから$^{58}$Coを分離できることが分かった。

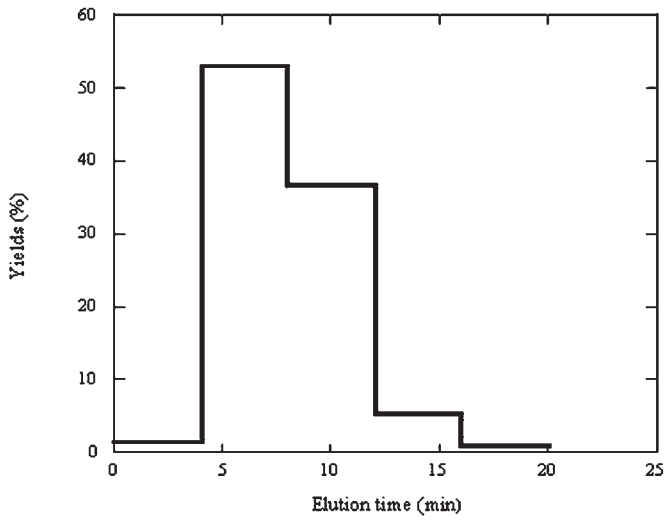


Fig.3.　Elution curve for Co. Flow rate of 1 M HF solution was 0.3 ml/min.

## §4　ま と め

KT結晶，KTN結晶中のMn，Fe，Co，Ni，Cu，Ptなどの不純物を分析するため，非破壊光量子放射化分析を検討した。その結果，マトリックスら生成する$^{181}$Taと$^{92m}$Nbの放射能強度が大きく非破壊分析が不可能であることが分かった。そこで，$^{58}$Coと$^{92m}$Nbをトレーサに用い，溶媒抽出とイオン交換分離を組み合わせた化学操作を検討した結果，$^{58}$Coを収率ほぼ100％で分離できる条件を明らかにした。

今後は，他の不純物元素に対する本分離操作の有用性を検討するとともに，放射化分析における収率補正法について検討を進める。

## 参　　考　　文　　献

[1] M. Sasaura *et al*.: J. Cryst. Growth **275** (2005) e2099.

[2] J.P. Paris: Anal. Chem. **32** (1960) 520.

[3] T. Ishimoti *et al*.: Bull. Chem. Soc. Japan **33** (1960) 636.

[4] S.M. Gasita *et al*.: Translated from Radiokhimiya, **26** (1984) 143.

[5] 日本化学会編著：新実験化学講座 1 （基本操作Ⅰ）(1975) 472.

(LNS Experiment: #2518, #2530)

# Distribution of $^{59}Fe$, $^{60}Co$ and $^{85}Sr$ as Low-level Radioactive Wastes Included in Nonflammable Organic Materials in the Decomposition by Supercritical Water with $RuO_2$

T. Yamamura[1], I. Satoh[1], W. Sugiyama[2], M. Takahashi[1],
Y. Shiokawa[1], H. Tomiyasu[3], and T. Ohtsuki[4]

[1] *Institute for Materials Research, Tohoku University, Sendai 980-8577*
[2] *Electric Power Research and Development Center, Chubu Electric Power Co., Inc., Nagoya 459-8522*
[3] *Department of Chemistry and Material Engineering, Faculty of Engineering, Shinshu University, Nagano 380-8553*
[4] *Laboratory for Nuclear Science, Tohoku University, Sendai 982-0826*

We investigated the distribution behavior of iron, cobalt and strontium attached to nonflammable organic materials, in solid, liquid and gas phases during the decomposition of these materials in supercritical water mixed with $RuO_2$. The distributions of these elements were determined by using their radioisotopes as simulated low-level radioactive wastes in order to ease the detection of trace amounts of elements even in solid and gas phases. The obtained results indicate that all of the elements investigated in this study (iron, cobalt, and strontium) can be recovered successfully by this supercritical-water process using $RuO_2$. Consequently, this process is suggested as a predominant candidate for the treatment of nonflammable organic materials in low-level radioactive wastes (LLW).

## §1. Introduction

Low-level radioactive wastes (LLW) generated at nuclear power plants can be classified into three categories in Japan: the wastes with (i) very low-level, (ii) relatively low-level and (iii) relatively high-level radioactivity. The conventional method for dealing with these wastes includes compression or incineration before solidification with mortar or concrete, and storing then in 200 L drum containers [1]. Even excluding the above-mentioned category (iii), more than half a million drum containers filled with LLW were being stored at domestic nuclear power plants by the end of FY 2001. One of the reasons why such a huge volume has accumulated is that the main components of the LLW are bulky nonflammable organic materials. No practical method for compressing or decomposing these wastes has been established yet and therefore volume reduction is not achieved satisfactorily.

A method using supercritical water with $RuO_2$ as a catalyst [2] was recently developed for achieving the complete gasification of nonflammable organic compounds, including even such compounds as stable aromatic structures. One of the most important applications of this method would be the decomposition of nonflammable organic materials contaminated with low-level radioactivity, in order to reduce their volume. We have reported on an investigation using this method to decompose nonflammable organic materials used in nuclear power plants [1]. For practical use, what is required is the removal of trace

quantities of radioactive elements attached to these plastics from gas and liquid phases and their concentration in the solid phase.

Radioisotopes contained in the LLW from nuclear power plants can be classified into two types by origin. One type is the radioactivated materials in nuclear power plants, *e.g.* iron-59 and cobalt-60 from the stainless steel (SUS) used as a major construction material, and the other is the fission products of uranium, such as strontium-90, which originate in the nuclear fuel, due to leakage.

In this study, the distribution of the above nuclides into solid, liquid and gas phases were investigated by applying the supercritical-water reaction with $RuO_2$ for decomposing the nonflammable organic materials. The objective of this study is to elucidate the optimum conditions for the concentration of the radionuclides into the solid phase. In order to detect trace quantities of elements even in the gas and solid samples collected after supercritical-water reaction, radiometric analysis was applied.

## §2. Experimental

Laminate sheeting, a popular product used in domestic nuclear power plants, is commercially available from Chiyoda Technol Corp., Japan. Reagents and radioactive reagents were used as purchased. Strontium-85, the tracer of strontium, was prepared by bremsstrahlung irradiation of $SrCO_3$ at the condition of 50 MeV, 100-120 $\mu$A, 8 hours with the electron linear accelerator (LINAC) at Laboratory of Nuclear Science, Tohoku University. Radioactive iron and cobalt hydroxides, as simulated radioactive scales of SUS, were prepared as follows already reported [3].

### 2.1 Supercritical-water reaction conditions

The supercritical batch-wise reactor made of hastelloy C-22 with a nominal inside volume of 10.8 $cm^3$ was supplied by Taiatsu Techno Corp., Japan. A certain amount of radioactive compound and non-radioactive carrier, 150 mg of laminate sheeting, 30 mg of $RuO_2$ and 3 mL of water were loaded into the above reactor. By using a temperature controller, the reaction condition of 450ºC-43 MPa was kept for 30 min.

After the reactor was cooled to room temperature, the volume of the gas produced by the supercritical-water reaction was measured using a gas pressure meter and the gas was collected in a 100 mL gas vial; then everything (liquid and solid phases) remaining inside the reactor was recovered and placed in a 10 mL polypropylene test tube. The inner surface of the reactor was rinsed with water three times (total 6 mL) and the washings were collected and added to the contents of the reactor. The supernatant liquid was separated into another polypropylene test tube by centrifuging these contents.

### 2.2 Determination of distribution factor

The radioactivity of $^{59}Fe$, $^{60}Co$, and $^{85}Sr$ were determined from the areas of their peaks at 1099.3, 1173.2, and 514.0 keV, respectively, by using the $\gamma$-ray spectrometer (GEM-28185-P, ORTEC Inc., USA). The distribution of their radioactivity in solid, liquid and gas phases was determined as given by

$$D_{phase} = \frac{A_{phase}}{A_T} \qquad (1),$$

where $D_{phase}$ designates the distribution ratio, $A_T$ and $A_{phase}$ are the total radioactivity of each phase after the supercritical-water reaction and the radioactivity of each phase respectively, and the subscription *phase* is "sol", "liq" or "gas", referring to the solid phase, the liquid phase and the gas phase, respectively.

## §3. Results and discussion

As reported previously [1], the laminate sheeting initially added is completely decomposed without any solid residues by the supercritical-water reaction using $RuO_2$. Also in this study, only the clear and colorless supernatant solutions and inorganic precipitates are recovered in the all runs. The gases produced during the decomposition of the laminate sheeting may consist of $CH_4$, $CO_2$ and $H_2$, according to our previous study [2]. Experimental conditions, the volume of the gas produced and the distribution in three phases in experiments on $^{59}$Fe, $^{60}$Co, and $^{85}$Sr are summarized in Table 1.

### 3.1 Distribution of $^{59}$Fe and $^{60}$Co

There is a tendency for the iron to precipitate almost quantitatively and only a trace amount is transferred to the liquid when a small amount of carrier is added (Table 1). The gas produced during the decomposition of the laminate sheeting contains no activity of $^{59}$Fe in any of the runs. This result indicates that both the decomposition of nonflammable plastics and the recovery of iron in the solid phase are successful. In contrast to the results for radioactive iron, about a quarter of $^{60}$Co distributes

Table 1. Distribution of Fe, Co, and Sr in three phases after reaction in supercritical-water of nonflammable plastics [3]

| Element | Carrier compound | Amount of carrier / mg | Tracer | Activity of tracer added / Bq | Amount of liquid phase / mL | Amount of gas phase / mL[3)] | $10^2D_{sol}$[2)] | $10^2D_{liq}$[2)] | $10^2D_{gas}$[2)] |
|---|---|---|---|---|---|---|---|---|---|
| Fe | $Fe(OH)_3$ | 0.13 [1)] | $^{59}$Fe | $3.12\times10^5$ | 9 | 90 | 97.5±1.5 | 2.5±0.0 | 0.0±0.0 |
| | | 1.3 [1)] | | $0.60\times10^5$ | 9 | 79 | 99.9±1.6 | 0.1±0.0 | 0.0±0.0 |
| | | 13 [1)] | | $2.94\times10^5$ | 9 | 70 | 100±1.4 | 0.0±0.0 | 0.0±0.0 |
| | | 130 [1)] | | $3.90\times10^5$ | 9 | 41 | 100±1.4 | 0.0±0.0 | 0.0±0.0 |
| Co | $Co(OH)_3$ | 2.3 [4)] | $^{60}$Co | $8.33\times10^4$ | 9 | 103 | 75.4±1.0 | 24.6±0.2 | 0.0±0.0 |
| | | 23 [4)] | | $9.02\times10^4$ | 9 | 90 | 76.7±0.8 | 23.3±0.2 | 0.0±0.0 |
| | | 230 [4)] | | $8.27\times10^4$ | 9 | 27 | 87.0±0.9 | 13.0±0.1 | 0.0±0.0 |
| Sr | $SrCO_3$ | trace | $^{85}$Sr | $8.21\times10^2$ | 9 | 65 | 15.1±0.4 | 84.9±1.2 | 0.0±0.0 |
| | | 5 | | $6.52\times10^3$ | 9 | 60 | 32.3±0.5 | 67.7±1.0 | 0.0±0.0 |
| | | 50 | | $2.97\times10^4$ | 9 | 44 | 78.0±0.3 | 22.0±0.1 | 0.0±0.0 |

1) Amount of $Fe(OH)_3$ calculated on the basis of the amount of $Fe(NO_3)_3\cdot9H_2O$ used to prepare $Fe(OH)_3$.
2) Value indicates measurement error [8].
3) Value calculated from gas pressure after reaction.
4) Amount of $Co(OH)_3$ calculated on the basis of the amount of $CoCl_2\cdot6H_2O$ used to prepare $Co(OH)_3$.

Table 2. Distribution of Co and Sr in three phases when 200 mg of non-radioactive iron hydroxide[1] was added for coprecipitation [3]

| Element | Carrier compound | Amount of carrier / mg | Tracer | Activity of tracer added / Bq | Amount of liquid phase / mL | Amount of gas phase / mL[3] | $10^2D_{sol}$[2] | $10^2D_{liq}$[2] | $10^2D_{gas}$[2] |
|---|---|---|---|---|---|---|---|---|---|
| Co | $CoCl_2 \cdot 6H_2O$ | not added | $^{60}Co$ | $2.19\times10^5$ | 9 | 27 | 98.5±0.9 | 1.5±0.0 | 0.0±0.0 |
| | | 5 | | $2.18\times10^5$ | 9 | 27 | 99.4±1.0 | 0.6±0.0 | 0.0±0.0 |
| Sr | $SrCO_3$ | 0.5 | $^{85}Sr$ | $2.66\times10^3$ | 9 | 20 | 7.3±0.1 | 92.7±1.0 | 0.0±0.0 |
| | $SrCO_3$ | 5 | | $4.55\times10^4$ | 9 | 21 | 91.7±0.3 | 8.3±0.10 | 0.0±0.0 |
| | $Sr(NO_3)_2$ | 5 | | $5.82\times10^3$ | 9 | 16 | 97.2±0.6 | 2.8±0.1 | 0.0±0.0 |

1) 200 mg of $Fe(OH)_3$ calculated on the basis of the 500 mg of $FeCl_3 \cdot 6H_2O$ used to prepare $Fe(OH)_3$.
2) Error indicates measurement error [8].
3) Value calculated from gas pressure after reaction.

to the liquid phase. In order to shift the distribution to the solid phase, 200 mg of non-radioactive iron hydroxide was added to the reactor and the supercritical-water reaction was examined (Table 2). Cobalt is quantitatively transferred to the solid phase, as seen only in the case of iron (Table 1). This dramatic improvement could be explained by the coprecipitation of the cobalt with the iron. The gas produced during the decomposition of laminate sheeting contains no activity of $^{60}Co$ in any run.

### 3.2 Distribution of $^{85}Sr$

Table 1 indicates that $^{85}Sr$ mainly stays in the liquid phase, and only a small amount is transferred to the solid phase, even when $SrCO_3$ carrier is added. The gas produced during the reaction contained no $^{85}Sr$ in any run. To recover radioactive strontium as a solid, two additional examinations were performed: (1) adding the non-radioactive iron hydroxide to the reactor before the reaction and (2) adding a precipitation reagent to liquid obtained after the reaction. In the case of examination (1), 200 mg of the non-radioactive $Fe(OH)_3$ was added to the reactor before the reaction (Table 2), and the strontium quantitatively transferred to the solid phase as seen only in the case of iron (Table 1). This dramatic improvement in the recovery of strontium in the solid phase could be explained by the coprecipitation of the strontium with the iron. In the case of examination (2), $Na_2CO_3$ or $NaHCO_3$ aqueous solution was added to radioactive $Sr(NO_3)_2$ aqueous solution as follows: A certain amount of non-radioactive $Sr(NO_3)_2$ as the carrier and $^{85}SrCO_3$ dissolved in a 1 M $HNO_3$ aqueous solution, which is the simulated solution obtained after the supercritical-water reaction, was mixed into 3 mL of water in a polypropylene test tube. By adding 1 mL of 0.4 M $Na_2CO_3$ or $NaHCO_3$ aqueous solution to the above-mentioned solution, a white suspension was obtained in all runs. After centrifuging, the supernatant liquid phase was transferred to another polypropylene test tube with a polyethylene dropper. The determined distribution of $^{85}Sr$ in this examination (Table 3) indicates that $Na_2CO_3$ and $NaHCO_3$ are excellent precipitate reagents for strontium. Thus, strontium dissolved in the liquid obtained after the supercritical-water reaction could be precipitated with $Na_2CO_3$ and $NaHCO_3$ aqueous solution.

Table 3. Distribution of Sr in solid and liquid phases after adding precipitation reagent to simulated solution obtained after reaction by supercritical-water mixed with $RuO_2$ [3]

| Element | Precipitate reagent | Carrier compound | Amount of carrier / mg | Tracer | Activity of tracer added / Bq | $10^2D_{sol}$ [1)] | $10^2D_{liq}$ [1)] |
|---|---|---|---|---|---|---|---|
| Sr | $Na_2CO_3$ [2)] | $Sr(NO_3)_2$ | 0.5 | $^{85}Sr$ | $5.03\times10^3$ | 99.1±0.7 | 0.9±0.0 |
| | $Na_2CO_3$ [2)] | | 5 | | $5.13\times10^3$ | 99.2±0.7 | 0.8±0.0 |
| | $NaHCO_3$ [2)] | | 0.5 | | $4.87\times10^3$ | 99.1±0.7 | 0.9±0.0 |
| | $NaHCO_3$ [2)] | | 5 | | $4.81\times10^3$ | 99.1±0.5 | 0.9±0.0 |

1) Error indicates measurement error [8].
2) Adding 1 mL of $Na_2CO_3$ or $NaHCO_3$ aqueous solution.

### 3.3 Precipitation mechanism in the case of Fe and Co

Under the conditions with small amounts (0.13 and 1.3 mg) of the non-radioactive iron hydroxide as the carrier, iron is not recovered in the solid completely and still remains in the liquid (Table 1). One possible explanation of these results is that the iron(III) could be simultaneously reduced to iron(II) during the reductive decomposition of the nonflammable organic materials. To obtain information on the oxidation state of the dissolved iron under these conditions, 2,2′-bipyridyl, a colorimetry reagent for $Fe^{2+}$, were added to the liquid obtained after the supercritical-water reaction with 0.13 and 1.3 mg of the non-radioactive iron hydroxide. The liquid turned pink and the absorption spectrum in the visible region showed an absorption band at 520 nm, which is attributed to $Fe^{2+}$ [4]. In the case of cobalt, the color of the liquid obtained after reaction was initially pale pink and changed to golden yellow when 2,2′-bipyridyl was added. Also non-radioactive condition, we prepared a cobalt(II) aqueous solution using $CoCl_2 \cdot 6H_2O$. The color of this solution was initially pale pink and changed to golden yellow when 2,2′-bipyridyl was added. These results indicated the production of $Fe^{2+}$ in the liquid by the reactions with 0.13 and 1.3 mg of the non-radioactive iron hydroxide and also $Co^{2+}$ in the liquid by supercritical-water reaction. These results show that iron(II) and cobalt(II) generated in the liquid after reaction. Iron and cobalt added into the reactor before the reaction was $Fe(OH)_3$ and $Co(OH)_3$, respectively. Therefore, iron(III) and cobalt(III) were respectively reduced to iron(II) and cobalt(II), and this means that a reductive mechanism is operating in the reaction using supercritical water mixed with $RuO_2$. It is worthwhile to note that the reduction of Co(III) to Co(II) requires very reductive conditions, as indicated by the standard electrode potential of -1.92 V vs. SHE [5] in comparison with that of Fe(III) to Fe(II), which is -0.771 V vs. SHE [5]. Once the divalent metal ion is formed, the cobalt(II) ion should have greater solubility than the iron(II) ion on the basis of the solubility product $K_{sp}$ obtained at the ambient temperature for $Fe(OH)_2$ and $Co(OH)_2$ $8\times10^{-16}$ [6] and $1.6\times10^{-15}$ [7], respectively.

Furthermore, all of the solids obtained after the supercritical-water reaction of iron showed ferromagnetism when checked with a magnet. Thus, a non-radioactive sample was prepared by the procedure wherein 200 mg of non-radioactive $Fe(OH)_3$, 30 mg of $RuO_2$, 150 mg of laminate sheeting and

3 mL of water reacted under standard conditions. The X-ray powder diffraction (XRD) was performed at RINT 2000 (Rigaku Corp., Japan) using $CuK_{\alpha 1}$. The XRD pattern of the obtained solid agreed very well with $Fe_3O_4$. Since the corresponding radioactive cobalt samples also exhibited ferromagnetic behavior, the non-radioactive sample was prepared by the same way of iron samples. the XRD pattern of the obtained solid agreed well with CoO. A detailed analysis of the solid obtained after the reaction using supercritical water mixed with $RuO_2$ is now underway.

With reference to the gasification mechanism proposed in ref. [2] for the decomposition of nonflammable organics using supercritical water with $RuO_2$ catalyst, the atmosphere of the supercritical-water reaction is suggested to be reductive. The above analysis of the solid phase obtained in the reaction also supports this reductive mechanism, where a portion of iron(III) and all of cobalt(III) are reduced to iron(II) and cobalt(II), respectively.

## §4. Summary

The present investigation indicates that during the decomposition of laminate sheeting, the produced gas contains no radioactivity in any run. The distribution of Fe, Co, and Sr was determined by radiometric analysis after laminate sheeting was decomposed using supercritical water mixed with $RuO_2$. Iron, cobalt and strontium were recovered as solids after the present supercritical-water reaction by the addition of an excessive quantity of iron hydroxide before the reaction. In the case of strontium, almost all radioactivities were found in the liquid phase. However, by adding precipitate reagents to the liquid phase obtained in the reaction, strontium can be recovered in the solid phase. This method should be a very effective way to decompose the nonflammable organic materials of LLW generated by nuclear power plants.

## References


[1] W. Sugiyama *et al*. : J. Nucl. Sci. Technol. **42** (2005) 256.

[2] K.-C. Park *et al*. : Chem. Commun. (2003) 694.

[3] W. Sugiyama *et al*. : J. Supercritical Fluid (2005) (Available online at doi:10.1016/ j.supflu.2005.02. 003).

[4] M.H. Ford-Smith *et al*. : J. Am. Chem. Soc. **83** (1961) 1830.

[5] A.J. Bard *et al*. : "*Standard Potentials in Aqueous Solutions*" , ed. ; IUPAC (Marcel Dekker): New York (1985).

[6] D.L. Leussing *et al*. : J. Am. Chem. Soc. **75** (75) 2476.

[7] A.O. Gübeli *et al*. : Helv. Chim. Acta **16** (1970) 1229.

[8] G. Gilmore: "*Practical Gamma-Ray Spectrometry*" , ed. ; John Wiley & Sons: Chichester, 1995.

# Ⅲ. List of Publication

# List of Publication（論文リスト）（2004.1～2004.12）

## Papers Published in Refereed Journals

Strongly Enhanced Li + D Reaction in Pd Observed for Deuteron Bombardment on PdLix with Energies between 30 and 75 keV.

J. Kasagi, Y. Yuki, T. Baba, A. Taguchi, M. Shimokawa, and W. Galster

J. Phys. Soc. Jpn. **73** (2004) 608-612.

Low energy nuclear reactions in metals.

J. Kasagi

Prog. Theor. Phys. Supp. **154** (2004) 365-372.

Nuclear Structure of the Spin-Isospin Excited States in $^{13}$N Studied via the ($^{3}$He, *t*) and ($^{3}$He, *tp*) Reactions at 450 MeV.

H. Fujimura, H. Akimune, I. Daito, M. Fujiwara, K. Hara, K.Y. Hara, M.N. Harakeh, F. Ihara, T. Inomata, K. Ishibashi, T. Ishikawa, T. Kawabata, A. Tamii, M. Tanaka, H. Toyokawa, T. Yamanaka, and M. Yosoi

Phys. Rev. **C69** (2004) 064327(1-11).

Isovector and Isoscalar Spin-flip M1 Strengths in $^{11}$B.

T. Kawabata, H. Akimune, H. Fujimura, H. Fujita, Y. Fujita, M. Fujiwara, K. Hara, K.Y. Hara, K. Hatanaka, T. Ishikawa , M. Itoh, J. Kamiya, S. Kishi, M. Nakamura, T. Noro, H. Sakaguchi, Y. Shimbara, H. Takeda, A. Tamii, S. Terashima, H. Toyokawa, M. Uchida, H. Ueno, T. Wakasa, Y. Yasuda, H.P. Yoshida, and M. Yosoi

Phys. Rev. **C70** (2004) 034318(1-10).

The Effect of Deformation in the Isoscalar Giant Dipole Resonance.

M. Itoh, H. Sakaguchi, M. Uchida, T. Ishikawa, T. Kawabata, T. Murakami, H. Takeda, T. Taki, S. Terashima, N. Tsukahara, Y. Yasuda, M. Yosoi, U. Garg, M. Hedden, B. Kharraja, M. Koss, B.K. Nayak, S. Zhu, H. Fujimura, M. Fujiawara, K. Hara, H.P. Yoshida, H. Akimune, M.N. Harakeh, and M. Volkerts

Nucl. Phys. **A731** (2004) 41-48.

Excitation and Decay of the Isovector Spin-flip Giant Monopole Resonance via the $^{208}$Pb ($^{3}$He, *tp*) Reaction at 410 MeV.

R.G.T. Zegers, H. Abend, H. Akimune, A.M. van den Berg, H. Fujimura, H. Fujita, Y. Fujita, M. Fujiwara, S. Gales, K. Hara, M.N. Harakeh, T. Ishikawa T. Kawabata, K. Kawase, T. Mibe, K. Nakanishi, S. Nakayama, H. Toyokawa, M. Uchida, T. Yamagata, K. Yamasaki, and M. Yosoi

Nucl. Phys. **A731** (2004) 121-128.

Cluster Fragmentations of Deep (1s)-hole States in Light nuclei.

M. Yosoi, H. Akimune, I. Daito, H. Ejiri, H. Fujimura, M. Fujiwara, K. Fushimi, K. Hara, K.Y. Hara, H. Hashimoto, T. Ishikawa, M. Itoh, Y. Itow, S. Kishi, T. Kawabata, K. Kawase,

M. Kinoshita, K. Kobayashi, M. Nakamura, K. Nakanishi, Y. Nakatsugawa, S. Nakayama, T. Noro, E. Obayashi, S. Okumura, H. Sakaguchi, Y. Sakemi, M. Shiozawa, H. Takeda, T. Taki, A. Tamii, M. Tanaka, S. Terashima, H. Toyokawa, N. Tsukahara, M. Uchida, T. Yamada, T. Yamagata, Y. Yasuda, H.P. Yoshida, R.G.T. Zegers, and J. Zenihiro
Nucl. Phys. **A738** (2004) 451-454.

Half-life of $^{7}$Be in Beryllium Metal.

T. Ohtsuki, H. Yuki, J. Kasagi, and M. Muto
Prog. Theor. Phys. Supp. **154** (2004) 392-396.

Enhanced Electron-Capture Rate of $^{7}$Be Encapsulated in **C60** Cages.

T. Ohtsuki, H. Yuki, M. Muto, J. Kasagi, and K. Ohno
Phys. Rev. Lett. **93** (2004) 112501 (1-4).

Technetium (IV) Oxide Colloids Produced by Radiolytic Reactions in Aqueous Pertechnetate Solution.

T. Sekine, H. Narushima, T. Suzuki, T. Takayama, H. Kudo, M. Lin, and Y. Katsumura
Colloids and Surfaces A: Physicochem. Eng. Aspects, **249** (2004) 105-109.

A Prebunched FEL Using Coherent Transition Radiation in the Millimeter Wave Region.

Y. Shibata, K. Ishi, T. Takahashi, T. Matsuyama, F. Hinode, and Y. Kondo
Nucl. Instrum. and Meth. Phys. Res. **A528** (2004) 162-166.

Observation of Millimeter-Wave Radiation Generated by the Interaction between an Electron Beam and a Photonic Crystal.

K. Yamamoto, R. Sakakibara, S. Yano, Y. Segawa, Y. Shibata, K. Ishi, T. Ohsaka, T. Hara, Y. Kondo, H. Miyazaki, F. Hinode, T. Matsuyama, S. Yamaguti, and K. Ohtaka
Phys. Rev. **E69** (2004) 045601 (R).

## Papers Published in International Conference Proceedings

Photoproduction of $\eta$ Mesons on Nuclei at LNS.

H. Yamazaki, T. Kinoshita, A. Katoh, T. Katsuyama, K. Kino, T. Nakabayashi, H. Shimizu, T. Terasawa, J. Kasagi, H. Kanda, K. Maeda, T. Takahashi, Y. Aruga, T. Fujinoya, A. Iijima, Y. Ito, T. Noma, Y. Tajima, H.Y. Yoshida, K. Hirota, T. Yorita, and O. Konno
Proceedings of the International Symposium "Electro-photoproduction of Strangeness on Nucleons and Nuclei", Edited by K. Maeda *et al*., World Scientific, (2004) 191--197.

Photoproduction of Neutral Kaons at LNS.

T. Takahashi, K. Dobashi, Y. Fujii, O. Hashimoto, K. Itoh, H. Kanda, M. Katoh, K. Maeda, A. Matsumura, H. Miyase, T. Miyoshi, K. Mizunuma, Y. Miura, S.N. Nakamura, H. Nomura, Y. Okayasu, T. Osaka, M. Oyamada, H. Tamura, H. Tsubota, K. Tsukada, M. Ukai, H. Yamauchi, M. Wakamatsu, T. Watanabe, T. Ishikawa, T. Kinoshita, F. Miyahara, H. Shimizu, T. Tamae, H. Terasawa, and H. Yamazaki
Proceedings of the International Symposium "Electro-photoproduction of Strangeness on Nucleons and Nuclei", Edited by K. Maeda *et al*., World Scientific, (2004) 198--207.

## Review

Giant Resonances in Light Nuclei via the (e,e′ n) Reaction.

T. Saito

Recent Res. Devel. Physics **5** (2004) 1057-1079.

# Ⅳ. Approved Experiments

# 平成16年度前期採択課題一覧表

| 課題番号 | 課　　題　　名 | 申込責任者 | 採　択<br>シフト数 |
|---|---|---|---|
| 原子核関連分野 | | | |
| 2506 | Photoproduction of Neutral Kaons on Liquid Deuterium Target | 橋本　　治 | 70 |
| 2507 | 低移行運動量領域における $^{40}$Ca(e, e'p) 反応の研究 | 玉江　忠明 | 28 |
| 2508 | 中性中間子光生成による原子核内核子共鳴状態の研究 | 山崎　寛仁 | 52 |
| 放射光関連分野 | | | |
| 2509 | フォトニック結晶からのスミス・パーセル放射スペクトル測定(3) | 近藤　泰洋 | 8 |
| 放射化学・物性関連分野 | | | |
| 2510 | 長寿命放射性核種の環境中移行における基礎化学反応研究 | 関根　　勉 | 2 |
| 2511 | ファイバアンプ用ガラス中の軽元素の光量子放射化分析 | 鹿野　弘二 | 1 |
| 2512 | 標識化による金属内包フラーレン及びヘテロフラーレンの研究及びその応用 | 大槻　　勤 | 3 |
| 2513 | Th-229m の製造と壊変特性の研究 | 中西　　孝 | 2 |
| 2514 | Th-229m の製造とその崩壊特性 | 三頭　聰明 | 1 |
| 2515 | 宇宙化学的試料および環境試料の光量子放射化分析 | 海老原　充 | 3 |
| 2516 | 電子ビームによるフリーラジカル生成の研究 | 結城　秀行 | 1 |
| 2517 | 金属及び半導体材料中の軽元素の定量のための分離・捕集法の開発 | 桝本　和義 | 2 |
| 2518 | 超臨界水中におけるストロンチウムの挙動 | 佐藤伊佐務 | 2 |
| 2519 | 水素誘起空孔による拡散の促進 | 山崎　仁丈 | 2 |

# 平成16年度後期採択課題一覧表

| 課題番号 | 課　　題　　名 | 申込責任者 | 採　択<br>シフト数 |
|---|---|---|---|
| 原子核関連分野 | | | |
| 2520 | $^{6}$Li, $^{7}$Li ( $\gamma$ , $\eta$) 反応による媒質効果の研究 | 石川　貴嗣 | 52 |
| 放射光関連分野 | | | |
| 2521 | フォトニック結晶からのスミス・パーセル放射スペクトル測定(4) | 近藤　泰洋 | 12 |
| 放射化学・物性関連分野 | | | |
| 2522 | 長寿命放射性核種の環境中移行における基礎化学反応研究 | 関根　勉 | 2 |
| 2523 | 光量子放射化分析法による光通信用材料中の不純物評価 | 鹿野　弘二 | 1 |
| 2524 | 標識化による金属内包フラーレン及びヘテロフラーレンの研究及びその応用 | 大槻　勤 | 3 |
| 2525 | Th-229m の製造と壊変特性の研究 | 中西　孝 | 1 |
| 2526 | Th-229m の製造とその崩壊特性 | 三頭　聰明 | 1 |
| 2527 | 宇宙化学的試料および環境試料の光量子放射化分析 | 海老原　充 | 3 |
| 2528 | 電子ビームによるフリーラジカル生成の研究 | 結城　秀行 | 1 |
| 2529 | 金属及び半導体材料中の軽元素の定量のための分離・捕集法の開発 | 桝本　和義 | 2 |
| 2530 | 超臨界水中におけるストロンチウムの挙動 | 佐藤伊佐務 | 2 |
| 2531 | 水素誘起空孔による拡散の促進 | 山崎　仁丈 | 1 |
| 2532 | DNA２本鎖切断の遺伝的影響；１倍体酵母と二倍体酵母の比較研究 | 山本　和生 | 2 |

**核理研研究報告　第38巻**

2005年11月発行

発行所　東北大学大学院理学研究科
附属原子核理学研究施設
仙台市太白区三神峯1-2-1（郵便番号982－0826）
電話　022－743－3400

印刷所　株式会社　東北プリント
仙台市青葉区立町24番24号
TEL　022（263）1166㈹

RESEARCH REPORT OF
LABORATORY OF NUCLEAR SCIENCE
TOHOKU UNIVERSITY

Volume 38 November 2005

Laboratory of Nuclear Science, Tohoku University,
1-2-1, Mikamine, Taihaku, Sendai 982-0826, Japan

東北大学大学院理学研究科

原 子 核 理 学 研 究 施 設